

# Slab morphology in the lower mantle and compositional segregation under different mantle-plate physical properties

Jingtao Min

June 2021

**Abstract** Subduction dynamics and consequent slab morphology depends on both mantle properties, phase transition constitutive parameters, and plate properties. Certain morphology of the subducted slab may be relevant to compositional segregation and recycling of the material. We use chemico-thermo-mechanical models to simulate free subduction of a surface plate initiated by temperature-induced negative buoyancy. Influence of different parameters on the morphology of the slab has been investigated, including 660 viscosity jump, upper-mantle activation volume, Clapeyron slope, initial age and plate yield strength. Two subduction regimes, (i) the strong-spreading regime, characterized by lateral spreading of subducted plate above 660km, before finally penetrating into the lower mantle, and (ii) the strong-penetration regime, characterized by slab's penetration of the 660 phase transition depth during lateral extension, have been identified. Each subduction regime results in different morphology of the slab as it sinks into the lower mantle. We show that upper-mantle activation volume and 660 Clapeyron slope play an important role in determining the specific dynamic regimes, while viscosity jump, initial plate age and yield strength seem to be irrelevant, at least within the range considered in this study. Similar compositional segregation and later dynamics near CMB develop for both regimes and slab morphology, and there is no simple clear-cut parameter difference which can be observed in this study that distinguishes stable basalt preservation near the CMB from the unstable cases.

## 1 Introduction

As a key part of plate tectonics, subduction of lithospheric plates as slabs provide essential ingredients to plate tectonics and mantle convection, and has profound effect on mantle dynamics. The negative buoyancy of the slab, referred to as slab pull, is recognized as the most important driving force for plate tectonics (Forsyth and Uyeda 1975). Subduction also provides the necessary force and dynamics for material transportation in the mantle, and is proposed to be the explanation for some mantle heterogeneities. For instance, it has long been proposed that accumulation of subducted material at the core-mantle boundary (CMB) gives rise to a chemically distinct and laterally heterogeneous layer (Christensen and Hofmann 1994), which is correlated with the D'' layer or large low shear velocity provinces (LLSVP) observed in seismology studies (Garnero and McNamara 2008, Dziewonski, Lekic, and Romanowicz 2010). Recently, it has also been postulated that subduction might also give rise to radial compositional layering, particularly in the mantle transition zone (MTZ) due to segregation of subducted oceanic slab and entrainment of depleted material in MTZ (Yan, Ballmer, and P. J. Tackley 2020). Therefore, subduction dynamics may be a key to understanding buildup of such chemical, thermal and mechanical heterogeneities in the mantle.

Compositional segregation of subducted plate and subsequent heterogeneity has already been produced in mantle convection models (Christensen and Hofmann 1994, P. J. Tackley 2011, Yan, Ballmer, and P. J. Tackley 2020). Using prescribed converging surface velocity field and subsequent subduction in 2D whole-mantle convection, Chirstensen and Hofmann (1994) shows that subducted oceanic crust can segregate at the bottom, and such heterogeneity can last long enough to develop isotopic signature. Tackley (2011) further studies different subduction geometries at CMB, and notes different segregation dynamics may be present depending on the geometry and orientation of the slab approaching CMB. Using a 2D global-scale convection model, Yan et al. (2020) shows recycling of the subducted plate results in basalt reservoirs inside MTZ, and harzburgite enrichment beneath MTZ. Some of the models assume certain subduction geometries or dynamics a priori (Christensen and Hofmann 1994, P. J. Tackley 2011). However, the exact morphology of the subducted slab is not constrained well enough. Different subduction styles have been proposed in geodynamic models (Garel et al. 2014), and seismic evidence also shows a variety of slab geometries (Fukao et al. 1992, C. Li et al. 2008). It is hence of importance to study how certain geometry of the slab is developed in the lower mantle.

Slab geometry and subduction dynamics are shaped by slab-mantle interaction during the subduction process. On one side of the interaction lie the mantle properties, where viscosity profile and phase transition parameters

have all been shown to affect the dynamics. Mantle viscosity is shown to affect compositional segregation and accumulation (Yan, Ballmer, and P. J. Tackley 2020). Parameters for phase transition, such as Clapeyron slope, are proposed to have a major role in controlling penetration of phase transition zone, particularly at 660km, or even dividing between whole-mantle convection and two-layer convection (Wolstencroft and Davies 2011).

On the other side of the interaction lie the slab/plate properties, including strength, yielding and thickness. For instance, flexural stiffness, a parameter consisting of effective viscosity and thickness, is shown to control the styles of subduction, whether in an advancing manner or in a folding-and-piling way above 660km (Stegman et al. 2010).

In order to analyze the effect of different parameters on slab morphology in the lower mantle, we systematically vary several parameters. For mantle properties, the upper-mantle activation volume  $V_\eta$ , the 660km viscosity jump  $\Delta\eta_{660}$ , and the Clapeyron slope of the 660km post-spinel phase transition  $\gamma_{660}$  are considered. The dependence of lower-mantle viscosity is not discussed in this study, which is justified by the simulation result that subduction dynamics and morphology are mostly modified in subduction phase and penetration phase, which either takes place in the upper mantle or MTZ, or is associated with transitions from MTZ to lower mantle. For plate properties, we consider initial temperature profile and ductile yield strength. We focus our choice on those parameters that are expected to influence the dynamics, and are subject to considerable uncertainties as well. For instance, initial temperature is dependent on spreading rate and plate length (2.3.1), which are all variable within certain range; data for Clapeyron slope come from experimental studies, but vary with specific mineral that is used (Ishii, Kojitani, and Akaogi 2011); activation volume has an ill name for its poor constraint because of extrapolation, and its uncertainty measured from a Bayesian approach ranges wider than its absolute value (Hirth and Kohlstedt 2004, Korenaga and S.-I. Karato 2008).

## 2 Method

### 2.1 Governing equations

We use the StagYY program to solve the equations for compressible anelastic flow with infinite Prandtl number. This is governed by the conservation of mass, the Stokes equation, and the heat equation:

$$\nabla \cdot (\rho \mathbf{u}) = 0 \quad (1)$$

$$-\nabla P + \nabla \cdot \boldsymbol{\sigma} + \rho g = 0 \quad (2)$$

$$\rho C_p \left( \frac{\partial T}{\partial t} + \mathbf{u} \cdot \nabla T \right) = \alpha T (\mathbf{u} \cdot \nabla P) + \nabla \cdot (k \nabla T) + \boldsymbol{\sigma} : \dot{\boldsymbol{\epsilon}} + \rho H \quad (3)$$

Density  $\rho$ , thermal conductivity  $k$  and thermal expansivity  $\alpha$  are initially calculated for a reference 1D profile, and then advected by Lagrangian tracers. The calculation of initial 1D profile of density or thermal properties implemented in this study is summarized in section 2.1.2.

The equation set (Eqn.1, 2, 3) is then equivalently 5 scalar equations about velocity field  $\mathbf{u}$ , pressure field  $P$ , stress field  $\boldsymbol{\sigma}$ , and temperature field  $T$ , in all 11 scalar variables (since strain rate tensor is by definition  $\dot{\boldsymbol{\epsilon}} = \frac{1}{2}(\nabla \mathbf{u} + (\nabla \mathbf{u})^T)$ ). This set of equations is then closed given appropriate constitutive relations between  $\boldsymbol{\sigma}$  and  $\mathbf{u}$ , which is summarized in the rheology part (section 2.1.1).

#### 2.1.1 Rheology

The constitutive relation is given by the equivalent stress - strain-rate relation:

$$\boldsymbol{\sigma}' = 2\eta\dot{\boldsymbol{\epsilon}} \quad (4)$$

In this study only diffusion creep is considered, and the stress-strain-rate relation is fully linear. The temperature- and pressure-dependent viscosity is described by Arrhenius law:

$$\eta(T, z) = \eta_0 \exp \left( \frac{E_\eta + pV_\eta}{RT} \right) \quad (5)$$

where activation energy  $E_\eta$  describes the negative dependence of viscosity on temperature, and activation volume  $V_\eta$  describes the positive dependence of viscosity on pressure.  $E_\eta$  and  $V_\eta$  are given for individual phases. Activation volume is a controlling factor of the viscosity gradient in the radial profile, and may have essential influence on slab morphology and subduction behavior. However, its inferred value, as described in previous studies (Hirth and Kohlstedt 2004, Korenaga and S.-I. Karato 2008), contains considerable uncertainties. In this study we vary this parameter systematically to study its influence on the slab geometry.

The reference-point viscosity  $\eta_0$  is also phase-dependent; instead of being prescribed, it is calculated from viscosity jumps/offsets at phase-change boundaries. These prescribed viscosity-jump factors  $\Delta\eta$  have strong effects on slab behavior during penetration of phase transition zones, and may give rise to different geometries of the slab. The viscosity jump at 660km, the depth at which transition to perovskite phase occurs, is varied and studied in this project.

In addition to phase, temperature and pressure, viscosity is also subject to brittle-/ductile-yielding, described by yielding strengths increasing linearly with pressure, similar in form to Byerlee's law:

$$\sigma_Y = \min(\sigma_{Y,\text{brittle}}, \sigma_{Y,\text{ductile}}), \quad \begin{cases} \sigma_{Y,\text{brittle}} = f_{\text{coh}} + \mu_{\text{brittle}} p \\ \sigma_{Y,\text{ductile}} = \sigma_{Y0} + \mu_{\text{ductile}} p \end{cases} \quad (6)$$

and the corresponding upper yielding bound for viscosity is calculated via  $\eta_Y = \sigma_Y / \dot{\varepsilon}_{II}$ , where  $\dot{\varepsilon}_{II}$  is the 2nd strain-rate invariant. Finally, the nonlinear viscosity is truncated by a lower bound  $\eta_{\min}$  and an upper bound  $\eta_{\max}$ .

### 2.1.2 Initial reference state

The initial density profile is calculated from a compression-dependent bulk modulus  $K_S$ , which is obtained from the 3rd-order Birch-Murnaghan equation of state:

$$K_S = -V \frac{dP}{dV} = -\frac{dP}{d\ln(V/V_0)} = \frac{dP}{d\ln(V_0/V)} = \frac{dP}{dx} \quad (7)$$

$$P = \frac{3}{2} K_{S0} \left( x^{7/3} - x^{5/3} \right) \left[ 1 + \frac{3}{4} (K'_S - 4) (x^{2/3} - 1) \right]$$

where  $x \equiv V_0/V$  denotes the compression ratio.  $K_{S0}$  and  $K'_S$  are the adiabatic bulk modulus and its pressure derivative at a given reference state (in this study assumed to be zero pressure and zero compression) respectively, and are prescribed for each phase.

The compression-dependent Grüneisen parameter  $\gamma$  is calculated via:

$$\gamma = \gamma_0 \left( \frac{\rho_0}{\rho} \right)^{q_\gamma} \quad (8)$$

where  $q_\gamma = 1.0$  is used, which then can be used to describe the thermal expansivity as a function of pressure, hence giving the initial thermal expansivity property field:

$$\alpha(P) = \frac{\rho(P)\gamma(P)c_p}{K_S(P)} \quad (9)$$

Finally, thermal conductivity is calculated by using a power-law dependence on density of thermal diffusivity, which gives

$$k = \rho c_p \kappa(\rho) = \rho c_p \kappa_0 \left( \frac{\rho}{\rho_0} \right)^{n_\kappa+1} \quad (10)$$

The initial temperature profile is described in section 2.3.

## 2.2 Numerical method

The model runs are produced using StagYY, a fortran program which solves equations of highly viscous flow using a finite difference/finite volume method on a staggered grid (P. J. Tackley 2008). Advection of some material properties such as composition and temperature is implemented using Lagrangian tracer particles.

At each timestep, a multi-grid iteration solver is used to solve for primitive kinematic and mechanical fields  $\mathbf{u}$  and  $p$ .

In this study, the program is run in a two-dimensional annulus sector domain. The specific model setup is discussed below.

## 2.3 Model setup

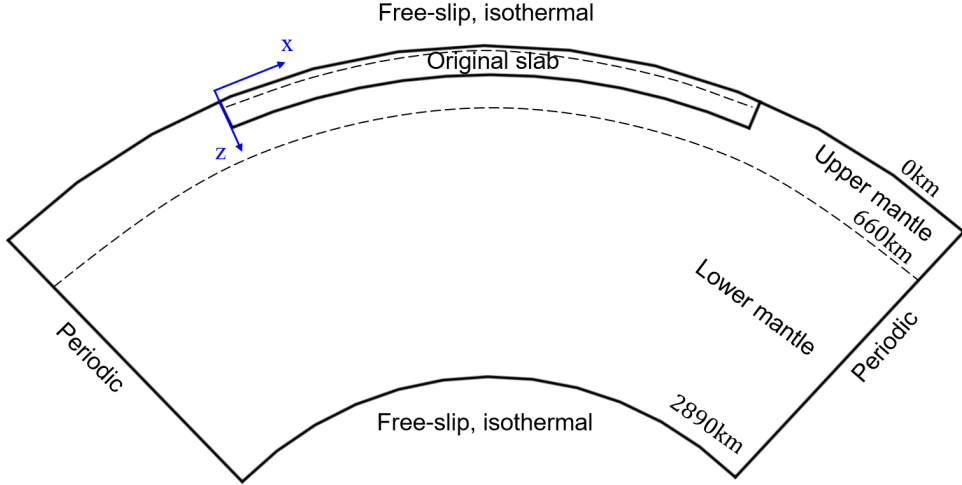


Figure 1: Schematic plot for the model used in the study

The initial model setup used in this study consists of a compositionally stratified, lower-temperature slab imposed at the surface of the domain on a reference background model, as schematically depicted in the figure 1. The domain is in the shape of a quarter sector of an annulus, i.e. an annulus sector with a central angle of  $45^\circ$ . The lower boundary of the domain corresponds to CMB, with an inner radius of 3480km; the upper boundary corresponds to the Earth surface, with an outer radius of 6370km. In most of the simulations, the domain is discretized laterally and radially into 256 and 128 nodal points respectively. The resolution is justified by the coherent result yielded by model run with this resolution (model STD, fig.3-6) and a model run with doubled resolution in both dimensions ( $512 \times 256$ , model STDRESp, fig.A1). The radial layers are finer near the surface and CMB, in order to capture finer features in the associated boundary layers.

### 2.3.1 Initial temperature profile

The fields and material properties of the background model, most of which are already summarized in 2.1.2, vary only radially. The background temperature profile assumes an interior potential temperature of  $T_{0,\text{init}} = 1600\text{K}$ , which is a reasonable value representative of today's Earth (Herzberg et al. 2007).

The slab at the surface features a different temperature profile, which is determined from the plate age, and further from the spreading velocity with the error function:

$$\begin{aligned} T_{\text{init}}^{\text{slab}}(x, z) &= T_{\text{surf}} + (T_{\text{init}} - T_{\text{surf}}) \operatorname{erf} \left( \frac{z}{2\sqrt{\kappa \operatorname{Age}(x)}} \right) \\ &= T_{\text{surf}} + (T_{\text{init}} - T_{\text{surf}}) \operatorname{erf} \left( \frac{z}{2\sqrt{\kappa x/v_{\text{spread}}}} \right) \end{aligned} \quad (11)$$

This gives a temperature profile of the plate which gradually increases from the surface temperature to the mantle temperature. Note the older the plate, the smaller the contribution of the error function, and hence colder the material. It is hence readily observed that the temperature at fixed depth decreases from the spreading centre ( $x = 0$ ) to the slab tip ( $x = L$ ), resulting in an isotherm that deepens towards the front of the plate. This temperature profile yields increasingly negative buoyancy towards the slab tip, which initiates the subduction. Also note that the age is inversely proportional to  $\sqrt{v_{\text{spread}}}$ . Therefore, a lower spreading velocity also results in more abundant cooling and more negative buoyancy.

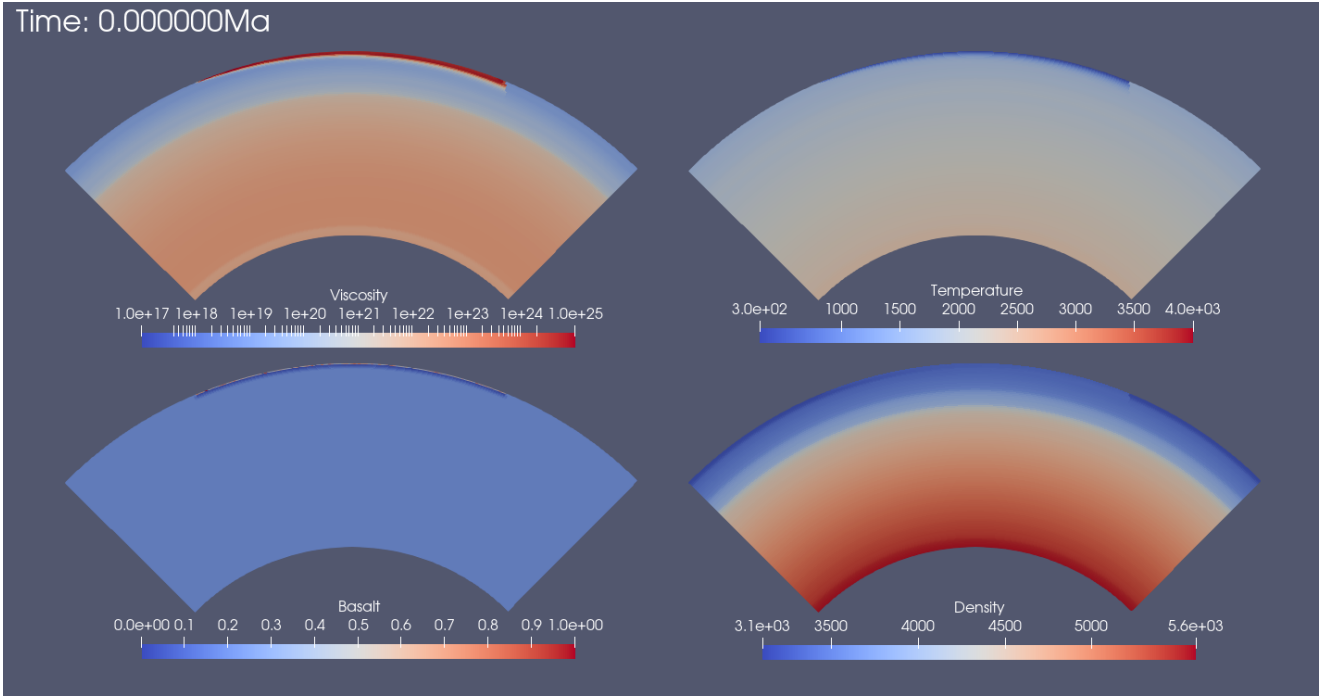


Figure 2: Setup of initial fields for reference model STD

### 2.3.2 Boundary conditions

For thermal boundary conditions, isothermal boundary conditions are implemented for the surface ( $T_{\text{surf}} \equiv 300\text{K}$ ) and CMB ( $T_{\text{CMB}} \equiv 4000\text{K}$ ). Free-slip condition is used as the mechanical boundary condition for lower boundary, and unless otherwise specified, also the mechanical boundary for the surface. A free-surface, implemented according to Duretz et al. (2016) allowing surface topography is used in a supplementary run for purposes of comparison (model FSDuretz, fig.A2), and is implemented by adding an air layer. Periodic boundary conditions are used for two sides, so that the flow and materials "wrap around" when reaching the boundary. This is used to avoid the unrealistic free-slip side boundaries, which often show channelling effects, facilitating upwellings and downwellings attached to the boundaries.

## 3 Results

The effect of several parameters on the morphology of the slab entering the lower mantle and eventually reaching the core-mantle boundary is studied by varying the parameters across a range of reasonable values. These parameters include:

- *upper mantle activation volume*  $V_\eta$ , and *viscosity jump factor* at 660km  $\Delta\eta_{660}$ , which control the upper mantle viscosity profile and its connection to lower mantle;  $\Delta\eta_{660}$  denotes the ratio of lower mantle viscosity to upper mantle viscosity, which are the viscosities just beneath and above the phase transition depth respectively.
- *Clapeyron slope* at 660km  $\gamma_{660}$ , which controls the buoyancy effect when slab is penetrating the phase transition at the bottom of the mantle transition zone;
- *initial state spreading velocity*  $v_{\text{spread}}$  of the slab, which controls the age, and hence the temperature profile in the slab, and consequently the slab strength;

In some cases, several other parameters are adjusted to maintain a reasonable level of viscosity profile across the mantle, although they are not of major interest in this study. These may include the reference viscosity  $\eta_0$  (viscosity at reference point, i.e. 1600K and 0 pressure at the surface phase, in Eqn. 5), the ductile yielding strength  $\sigma_{Y0}$ .

Several output parameters, hereafter referred to as diagnostic outputs, are extracted from model snapshots and time series, so as to enable quantitative description of the models. These output parameters include:

- *Slab front depth*  $h(t)$ . This time series is obtained by tracking the depth of the lowermost grid below certain temperature threshold, in this case 1300K. From the  $h(t)$  time series it is then ready to extract:
- *Slab sinking time when it reaches 660-discontinuity*  $t_{660}$ .
- *Trench location*  $x(t)$ . This time series is obtained by tracking the horizontal position of the surface point with highest convergence (i.e. most negative velocity difference). Combining the  $x(t)$  time series and  $t_{660}$  it is then ready to extract:
- *Trench migration when it reaches 660-discontinuity*  $x_{660}$ .
- *Average basalt content above CMB*  $\bar{C}_{\text{CMB}}(t)$ . This time series is obtained by calculating the mean of composition index of several layers (corresponding to 150km thickness) right above the CMB, weighted by layer grid thicknesses.

Table 1: Parameters for model STD

| Quantity                       | Symbol                                 | Unit                            | Value                 |
|--------------------------------|--|---------------------------------|-----------------------|
| Gravity                        | $g$                                    | $\text{m s}^{-2}$               | 9.81                  |
| Molar gas constant             | $R$                                    | $\text{JK}^{-1}\text{mol}^{-1}$ | 8.314462618           |
| Annulus inner radius           | $r_{\text{CMB}}$                       | km                              | 3480                  |
| Annulus outer radius           | $r_{\oplus}$                           | km                              | 6370                  |
| Domain width (longitude)       | $\phi$                                 | rad                             | 1.57                  |
| Internal heating rate          | $R_h$                                  | $\text{W m}^{-3}$               | $5.2 \times 10^{-12}$ |
| Surface temperature            | $T_{\text{surf}}$                      | K                               | 300                   |
| CMB temperature                | $T_{\text{CMB}}$                       | K                               | 4000                  |
| Mantle potential temperature   | $T_0$                                  | K                               | 1600                  |
| Reference viscosity            | $\eta_0$                               | $\text{Pa} \cdot \text{s}$      | $1 \times 10^{19}$    |
| Ductile yield strength         | $\sigma_{Y,0}$                         | MPa                             | 20.0                  |
| Ductile strength gradient      | $\mu_{\text{ductile}}$                 | —                               | 0.01                  |
| Plate spreading rate           | $v_{\text{spread}}$                    | $\text{cm yr}^{-1}$             | 3.0                   |
| Equivalent slab-tip age        | $\text{Age}_{\max}$                    | Myr                             | 166.7                 |
| <b>Olivine system*</b>         |  |                                 |                       |
| Surface density                | $\rho_{\text{surf}}^{\text{Ol}}$       | $\text{kg m}^{-3}$              | 3240                  |
| Surface thermal expansivity    | $\alpha_{\text{surf}}^{\text{Ol}}$     | $\text{K}^{-1}$                 | $3.10 \times 10^{-5}$ |
| Surface thermal conductivity   | $k_{\text{surf}}^{\text{Ol}}$          | $\text{W m}^{-1}\text{K}^{-1}$  | 2.95                  |
| Upper-mantle activation volume | $V_{\eta}^{\text{UM}}$                 | $\text{cm}^3 \text{mol}^{-1}$   | 5.0                   |
| 660 viscosity jump             | $\Delta\eta_{660}$                     | —                               | 3.0                   |
| 660 Clapeyron slope            | $\gamma_{660}$                         | $\text{MPa K}^{-1}$             | -2.5                  |
| <b>Pyroxene-Garnet system*</b> |  |                                 |                       |
| Surface density                | $\rho_{\text{surf}}^{\text{Py-Grt}}$   | $\text{kg m}^{-3}$              | 3080                  |
| Surface thermal expansivity    | $\alpha_{\text{surf}}^{\text{Py-Grt}}$ | $\text{K}^{-1}$                 | $2.95 \times 10^{-5}$ |
| Surface thermal conductivity   | $k_{\text{surf}}^{\text{Py-Grt}}$      | $\text{W m}^{-1}\text{K}^{-1}$  | 2.80                  |
| Upper-mantle activation volume | $V_{\eta}^{\text{UM}}$                 | $\text{cm}^3 \text{mol}^{-1}$   | 5.0                   |

\*unless otherwise specified, parameters for these phase systems, including activation volumes, activation energies, Clapeyron slopes, and density changes all follow those used in P. Tackley et al. 2013.

### 3.1 From subduction to lower mantle: dynamics of a reference model

The general evolution of the numerical model is illustrated below, using a reference model (model STD, fig.3, 5 and 6). Activation volume  $V_{\eta} = 5 \times 10^{-6} \text{ m}^3 \text{mol}^{-1}$  for all phases in upper mantle, viscosity jump at

660km  $\Delta\eta_{660} = 3.0$ , and Clapeyron slope  $\gamma_{660} = -2.5 \text{ MPa K}^{-1}$ . A spreading velocity of  $3\text{cm yr}^{-1}$  is used, corresponding to a slab age increasing linearly from 0yr at the spreading centre to 167Myr at the tip, where subduction is initiated. Other model parameters are collected in table 1.

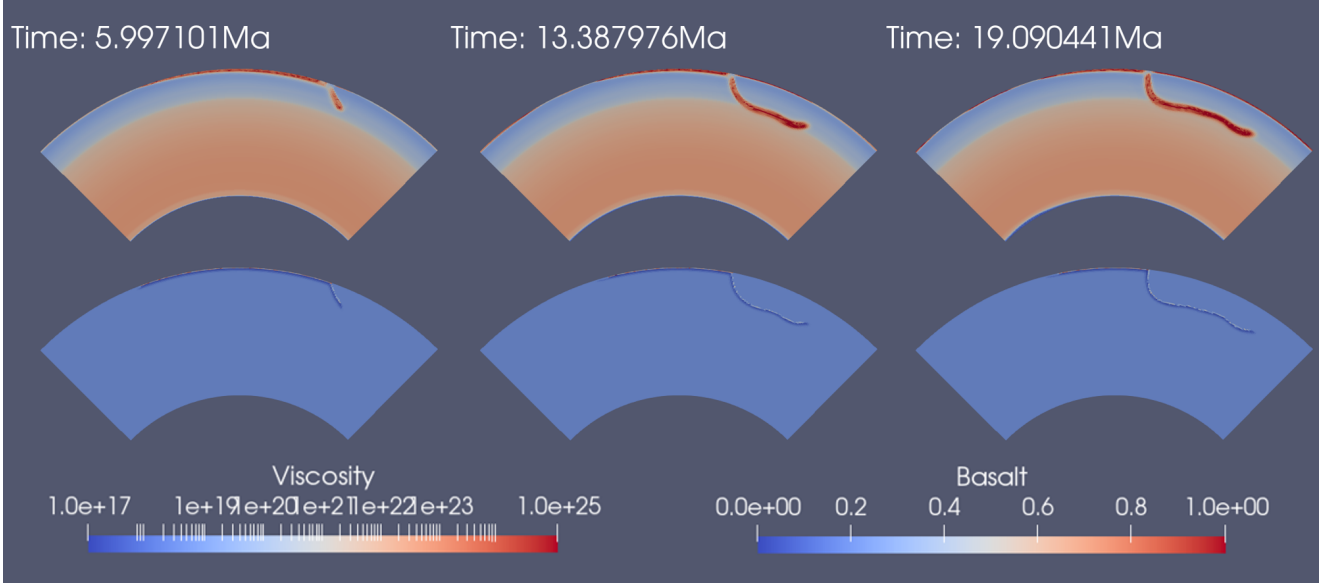


Figure 3: Snapshots of model STD during subduction. Upper panel shows the viscosity fields, and the lower panel shows the composition fields for each time step. Composition field is given by an index of basalt content ranging from 0 to 1

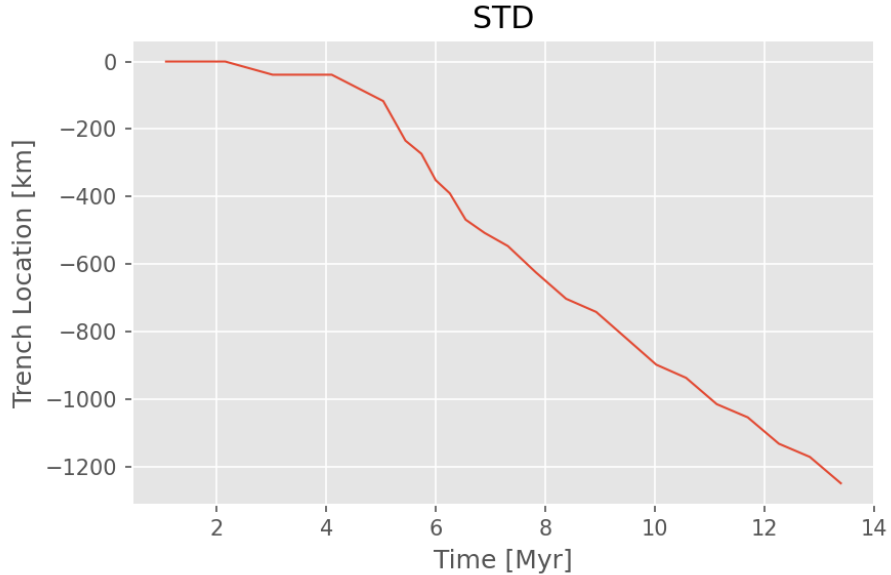


Figure 4: Trench motion for model STD. Initial trench location is defined as 0, and the positive direction is defined as in fig. 1

Due to the prescribed compositional and temperature initial state, the slab at the surface shows higher density compared to its surroundings. Such negative buoyancy then initiates the subduction, without the help of any facilitating geometry or boundary condition. An inclined subduction is initiated, with an inclination angle around  $45^\circ$  as the slab sinks into the upper mantle, as is the case in all model runs. This process lasts until around 7.5Myr, when the slab "feels" the resistance due to increased viscosity at 660km and gets deflected. This time point is close to the diagnostic output  $t_{660} \approx 8.3\text{Myr}$ , which is obtained by tracking the time when 1300K contour reaches 660km.

From  $7 \sim 8\text{Myr}$  onwards, the slab extends laterally above the 660-discontinuity, before it finally sinks into

the lower mantle around 20Myr. In absence of consistent melting and crust production, the slab floating horizontally above the 660-discontinuity reaches up to 3000km, which is 60% the original slab length. It should also be noted that this period is accompanied by very rapid trench retreat, with an average trench retreat velocity of over 9 cm yr<sup>-1</sup> (fig.4).

The evolution described above, starting from subduction, and ending with initiation of 660 penetration, is hereafter referred to as phase I / subduction phase.

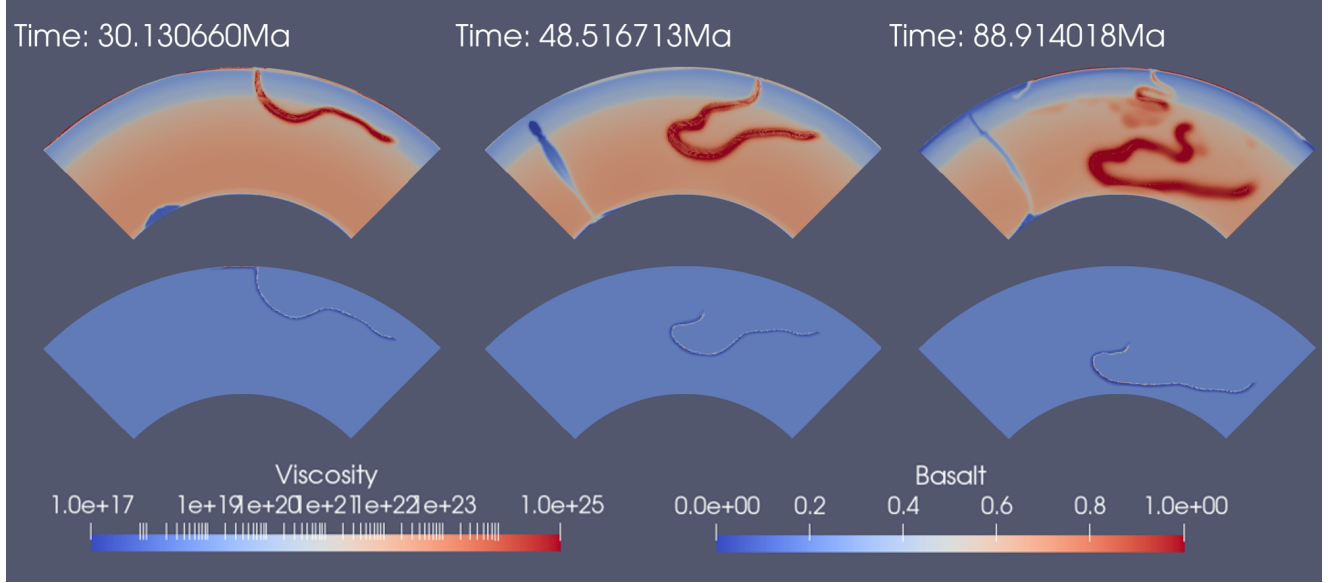


Figure 5: Snapshots of model STD during penetration. Upper panel and lower panel show the same fields as fig.3

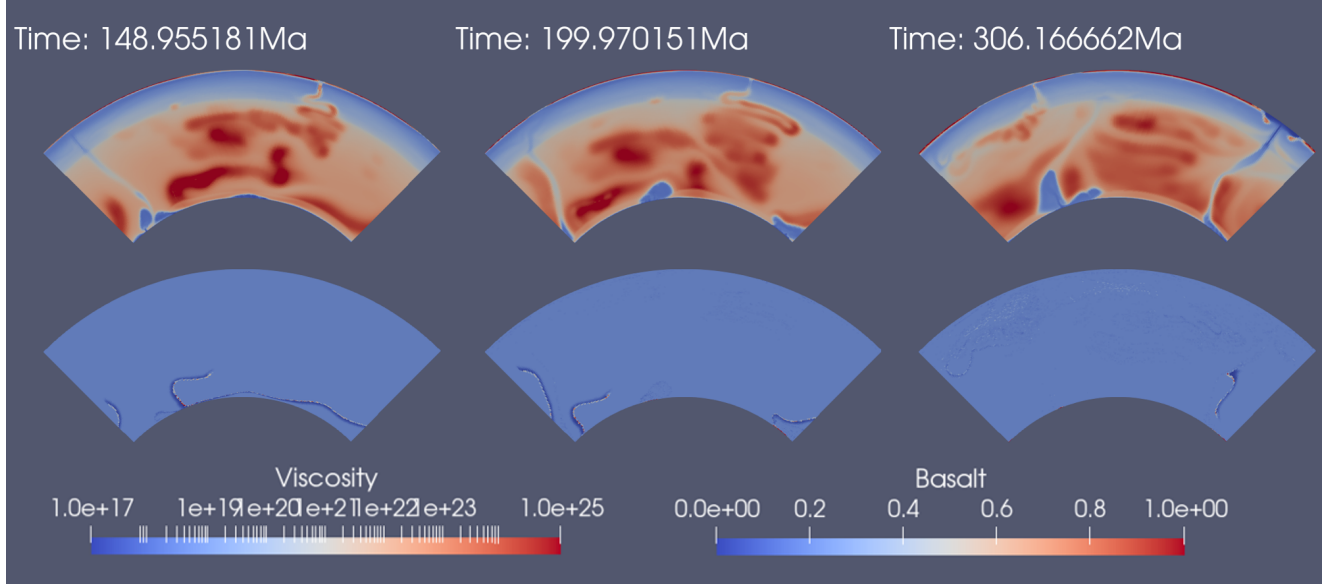


Figure 6: Snapshots of model STD at CMB. Upper panel and lower panel show the same fields as fig.3

The penetration of the 660-discontinuity, or slab's sinking into the lower mantle, occurs after 20Myr. This phase, hereafter referred to as phase II / penetration phase, reshapes the slab geometry, and is the controlling factor of geometry of slabs approaching CMB. In this example, the penetration begins with sinking of the latter part of the horizontal slab at 660km, and curvature develops as the penetration proceeds. Note at this stage the trench retreat has slowed down significantly, and consequently the subduction has transitioned to steep-angle near-vertical subduction, which might facilitate slab penetration. As slab at the surface diminishes, the subduction seems to be affected by compensational flow in the upper mantle, and the trench motion transitions from retreat to advance from 30Myr. This results in forward folding of the final part of the slab,

and the slab takes a dipper-shaped geometry when sinking into the lower mantle (fig.5, 48.5Myr snapshot). The slab enters phase III / lower-mantle phase when the entire plate sinks into the lower mantle (fig.5 88.9Myr snapshot and fig.6). Dynamics in the lower mantle is simpler compared to the change of morphology in the upper mantle. As the viscosity is 1-2 orders of magnitudes higher than in upper mantle, the slab sinking is considerably slower. The sinking motion is also strongly correlated with plume bursts, as is observed in many cases. Without major viscosity discontinuities and with relatively high strength of the slab, the slab generally retains the original geometry it has when it first sinks into the lower mantle. Moderate modifications may be present, including smoothening, flattening and relief of some local curvatures. Therefore, the slab morphology at the end of phase II is representative or at least indicative of the geometry of the slab approaching CMB.

In this illustration model, the folded final part of the slab is conserved when the slab approaches CMB, and is hence mechanically stable since the heavy basalt is turned downwards. The middle part of the dipper, which is mildly concave when it first enters the lower mantle (fig.5 48.5Myr snapshot), flattens out into a low-angle flat slab (fig.5 88.9Myr snapshot).

Table 2: Key parameters for models discussed

| Model name  | Difference from STD (non-standard parameters)  |
|-------------|--|
| CLmed       | $\gamma_{660} = -2.0 \text{ MPa K}^{-1}$   |
| CLm         | $\gamma_{660} = -1.5 \text{ MPa K}^{-1}$   |
| CLO         | $\gamma_{660} = 0.0 \text{ MPa K}^{-1}$  |
| Vmed        | $V_\eta^{\text{UM}} = 4.0 \text{ cm}^3 \text{ mol}^{-1}$   |
| Vmmmed      | $V_\eta^{\text{UM}} = 3.5 \text{ cm}^3 \text{ mol}^{-1}$   |
| Vm          | $V_\eta^{\text{UM}} = 3.0 \text{ cm}^3 \text{ mol}^{-1}$   |
| Vmm         | $V_\eta^{\text{UM}} = 2.5 \text{ cm}^3 \text{ mol}^{-1}$   |
| VmedCLmed   | $V_\eta^{\text{UM}} = 4.0 \text{ cm}^3 \text{ mol}^{-1}, \gamma_{660} = -2.0 \text{ MPa K}^{-1}$                       |
| VmedCLm     | $V_\eta^{\text{UM}} = 4.0 \text{ cm}^3 \text{ mol}^{-1}, \gamma_{660} = -1.5 \text{ MPa K}^{-1}$                       |
| VmmmedCLmed | $V_\eta^{\text{UM}} = 3.5 \text{ cm}^3 \text{ mol}^{-1}, \gamma_{660} = -2.0 \text{ MPa K}^{-1}$                       |
| VmmmedCLm   | $V_\eta^{\text{UM}} = 3.5 \text{ cm}^3 \text{ mol}^{-1}, \gamma_{660} = -1.5 \text{ MPa K}^{-1}$                       |
| VmCLO       | $V_\eta^{\text{UM}} = 3.0 \text{ cm}^3 \text{ mol}^{-1}, \gamma_{660} = 0.0 \text{ MPa K}^{-1}$                        |
| App         | $v_{\text{spread}} = 1.0 \text{ cm yr}^{-1}, \text{Age}_{\max} = 500 \text{ Myr}$                                      |
| Ap          | $v_{\text{spread}} = 2.0 \text{ cm yr}^{-1}, \text{Age}_{\max} = 250 \text{ Myr}$                                      |
| Am          | $v_{\text{spread}} = 4.0 \text{ cm yr}^{-1}, \text{Age}_{\max} = 125 \text{ Myr}$                                      |
| VmEOp       | $V_\eta^{\text{UM}} = 3.0 \text{ cm}^3 \text{ mol}^{-1}, \eta_0 = 10^{20} \text{ Pa s}$                                |
| VmEOpSYm    | $V_\eta^{\text{UM}} = 3.0 \text{ cm}^3 \text{ mol}^{-1}, \eta_0 = 10^{20} \text{ Pa s}, \sigma_{Y,0} = 20 \text{ MPa}$ |

### 3.2 Influence of viscosity profile

As discussed in the beginning of section 3, several parameters are varied systematically in order to study their effects. These models with perturbed parameters are collected in table 2.

Two parameters that play a controlling role in determining the reference state viscosity profile are varied in this study. The 660 viscosity jump factor  $\Delta\eta_{660}$ , defined as the ratio of the viscosity beneath and above the 660-discontinuity, controls the viscosity contrast between lower mantle and upper mantle. The upper-mantle activation volume  $V_\eta$ , which is the multiplier of pressure in the Arrhenius law (eqn.5), controls the increase of viscosity with pressure, and thus is the major contributor to the radial pressure gradient in the upper mantle.

Varying two parameters can alter the viscosity profile significantly. Note that variation in upper-mantle  $V_\eta$  also affects the lower-mantle viscosity, as it controls the viscosity right above 660km  $\eta_{660-}$ , and the lower-mantle viscosity is calculated with  $\Delta\eta_{660}$ . Also note that the viscosity contrast is not exclusively controlled by the 660 viscosity jump  $\Delta\eta_{660}$ , because of the nontrivial pressure-dependence of viscosity also in the lower mantle. Therefore, even with a trivial  $\Delta\eta_{660} = 1$  or  $\eta_{660-} = \eta_{660+}$ , the overall viscosity contrast between lower and upper mantle is still significant, typically on the order of  $10^1 \sim 10^2$ .

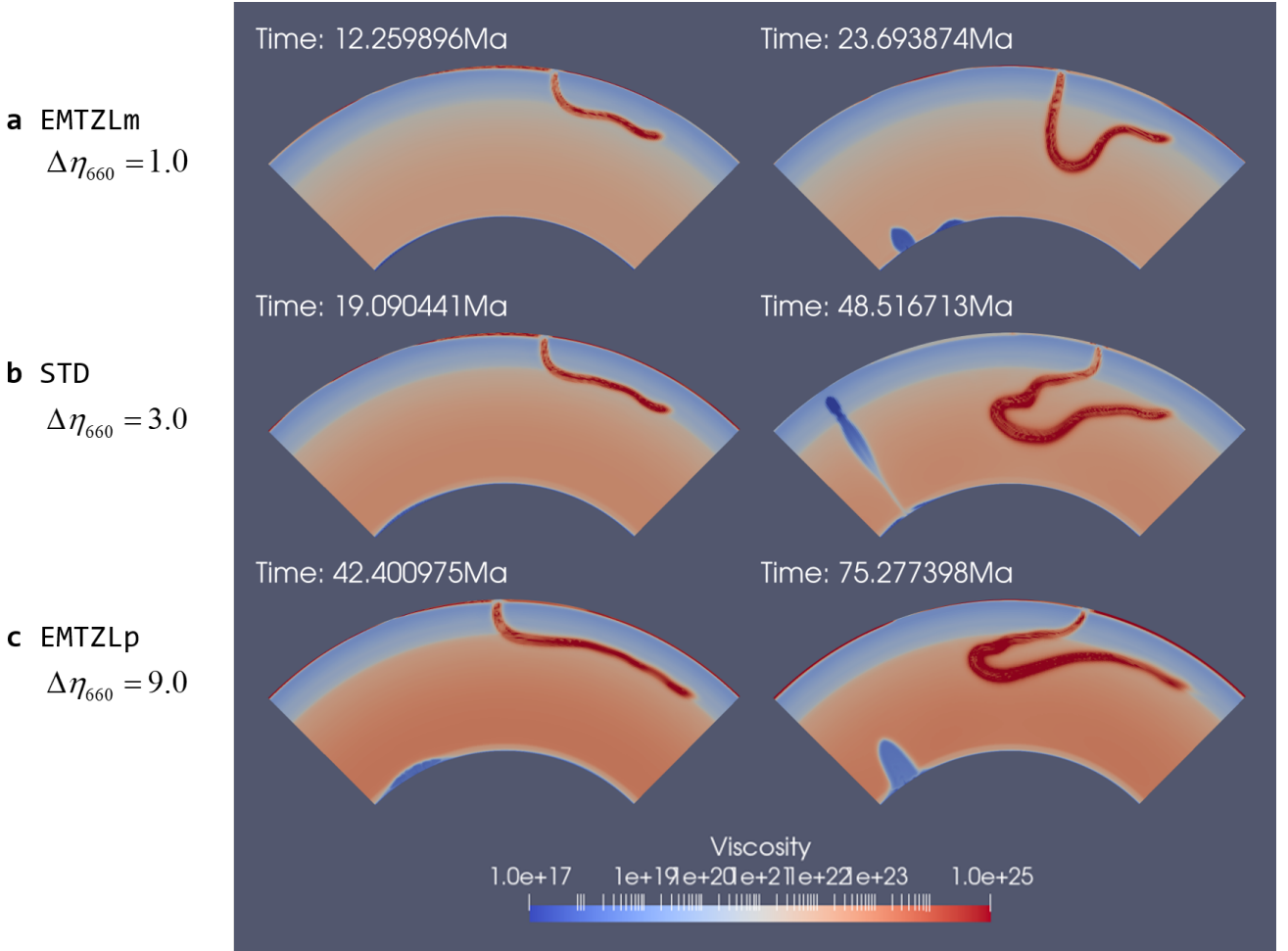


Figure 7: Snapshots of viscosity fields for models with different  $\Delta\eta_{660}$ . Each row shows evolution of one model during phase I-II.

### 3.2.1 660 viscosity jump factor $\Delta\eta_{660}$

Simulations show that varying the 660 viscosity jump alone within range 1.0 to 9.0 does not change the general dynamics in subduction phase or the penetration phase. The models always begin with inclined subduction, as the upper-mantle viscosity profile is basically not affected by the viscosity jump. The slabs always extend laterally above the 660-discontinuity without direct penetration, even when no sudden viscosity discontinuity is prescribed ( $\Delta\eta_{660} = 1.0$ ). The penetration always begins with the sinking of the latter part, which is the junction segment between the frontal horizontal slab and the subduction slab from the trench, and always results in curving and bending of the latter part, giving the slab its dipper shape.

Several differences arise from different 660 viscosity jumps. In the subduction phase, models with higher 660 viscosity jump delay the initiation of penetration phase, and are able to accommodate longer horizontal slab in MTZ before penetration (model EMTZLp, fig. 7-c).

Penetration phases for different  $\Delta\eta_{660}$  feature different curvatures, probably due to different lower-mantle viscosity. Models with higher  $\Delta\eta_{660}$  are more viscous in lower mantle, which slows down the sinking process. With the help of upper-mantle return flows, high  $\Delta\eta_{660}$  models develop greater curvature at the junction point or even folding of the final part of the lab onto the first-subducted part. Therefore, high  $\Delta\eta_{660}$  cases result in strongly curved scoop, close to a hairpin, while low  $\Delta\eta_{660}$  cases result in deeper and larger scoops of the dipper.

Due to higher lower-mantle viscosity and longer slab, the model with  $\Delta\eta_{660} = 9.0$  is free from significant segmented compositional segregation, and the entire subducted slab mostly acts as a whole even after 400Myr of model run. In comparison, lower viscosity jump models typically show thinning at points with high curvature and breaking into multiple segments, which segregates dense basalt onto the CMB separately afterwards. Due

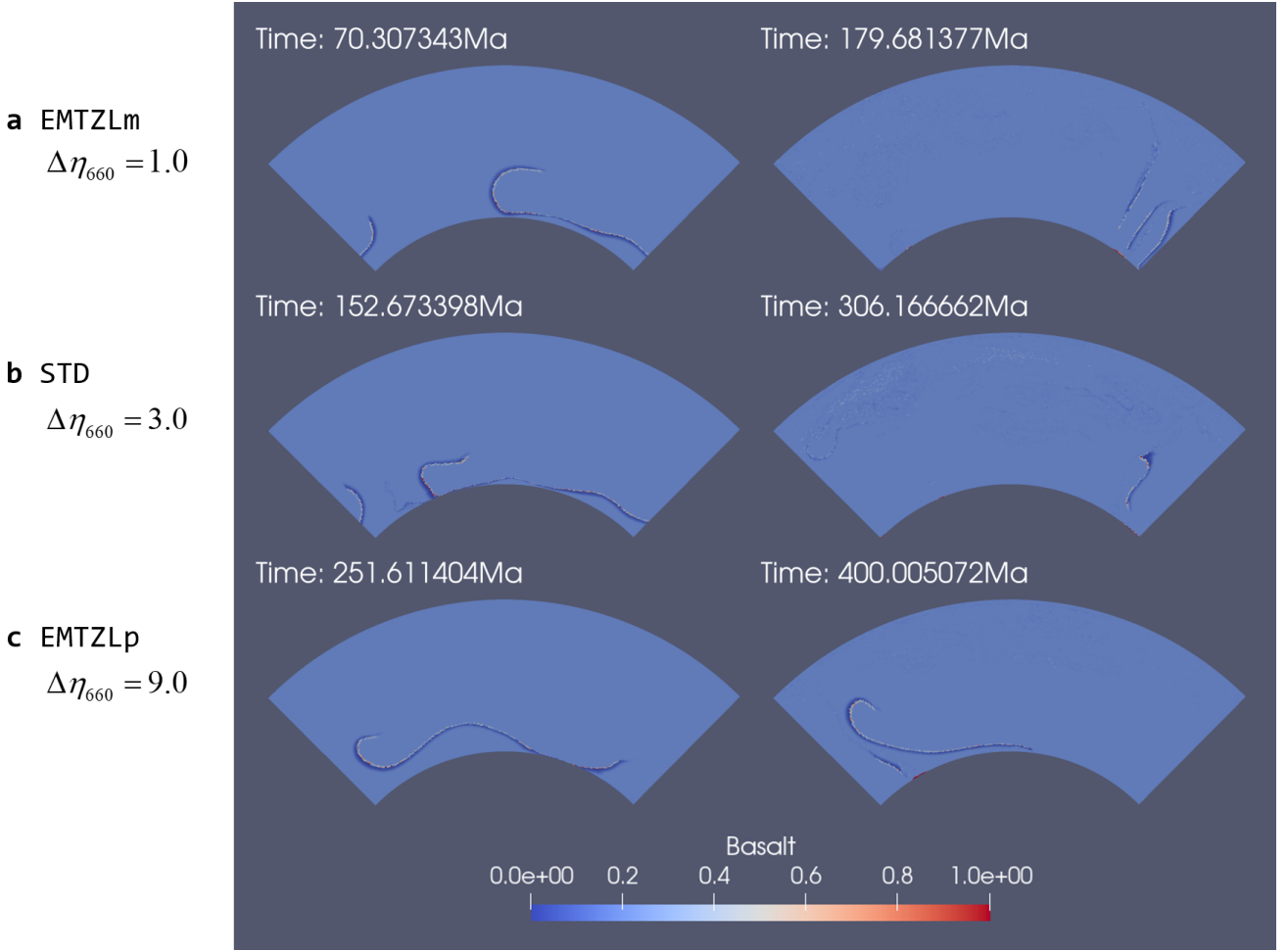


Figure 8: Snapshots of composition fields for models with different  $\Delta\eta_{660}$ . Each row shows evolution of one model during later evolution at CMB. Composition fields are visualized for later stages to show segregation.

to upwelling harzburgite flows, the mechanically unstable compositional structures are often turned to reorient vertically (see models EMTZL<sub>m</sub> and STD, fig. 8-a, b).

### 3.2.2 Upper-mantle activation volume $V_\eta$

Our models show that geometry of the slabs at the end of the penetration phase is sensitive to upper-mantle activation volume  $V_\eta$ . This comes as a surprise, as penetration takes place near the 660-discontinuity and the uppermost lower mantle, instead of inside the bulk region of upper mantle. One significant transition occurs when the activation volume drops to or below  $V_\eta = 3 \times 10^{-6} \text{ m}^3 \text{ mol}^{-1}$  (model V<sub>m</sub> and V<sub>mm</sub>, fig. 9-a,b). In these cases, no exclusive stage is observed for lateral slab accumulation above the 660-discontinuity; instead, deflection at the 660-discontinuity and penetration take place almost at the same time.

As a result of more direct penetration, sinking occurs for the entire slab around the same time, instead of beginning with the latter part. The localized curvature is then replaced by a smoother curve, which gives a blow-shaped slab at the end of the penetration phase, where the initial deflected part and the final subducted part serve as walls of the bowl (model V<sub>m</sub> and V<sub>mm</sub>, fig. 9-a,b). Thinning occurs at the junction of walls and bottom of the slab, breaking the slab into segments, which are gradually reoriented vertically while segregating basalt downwards and harzburgite upwards, similar to the reference model.

Subduction and penetration are very rapid in low  $V_\eta$  cases. In the case of  $V_\eta = 3 \times 10^{-6} \text{ m}^3 \text{ mol}^{-1}$ , phase II ends around 7.5Myr, compared to 45Myr with a reference activation volume  $V_\eta = 5 \times 10^{-6} \text{ m}^3 \text{ mol}^{-1}$ . This is expected as both the upper-mantle and lower-mantle viscosities are significantly reduced by a lower  $V_\eta$ . In comparison, when a higher  $\eta_0$  is used to adjust the lower-mantle viscosity back to reference state, the ending time of phase II returns to 48Myr (model V<sub>mE0p</sub>, fig. 10). One might suspect that the deviation of the geometry also arises simply from lower viscosity. This is not the case, however, as supplementary model

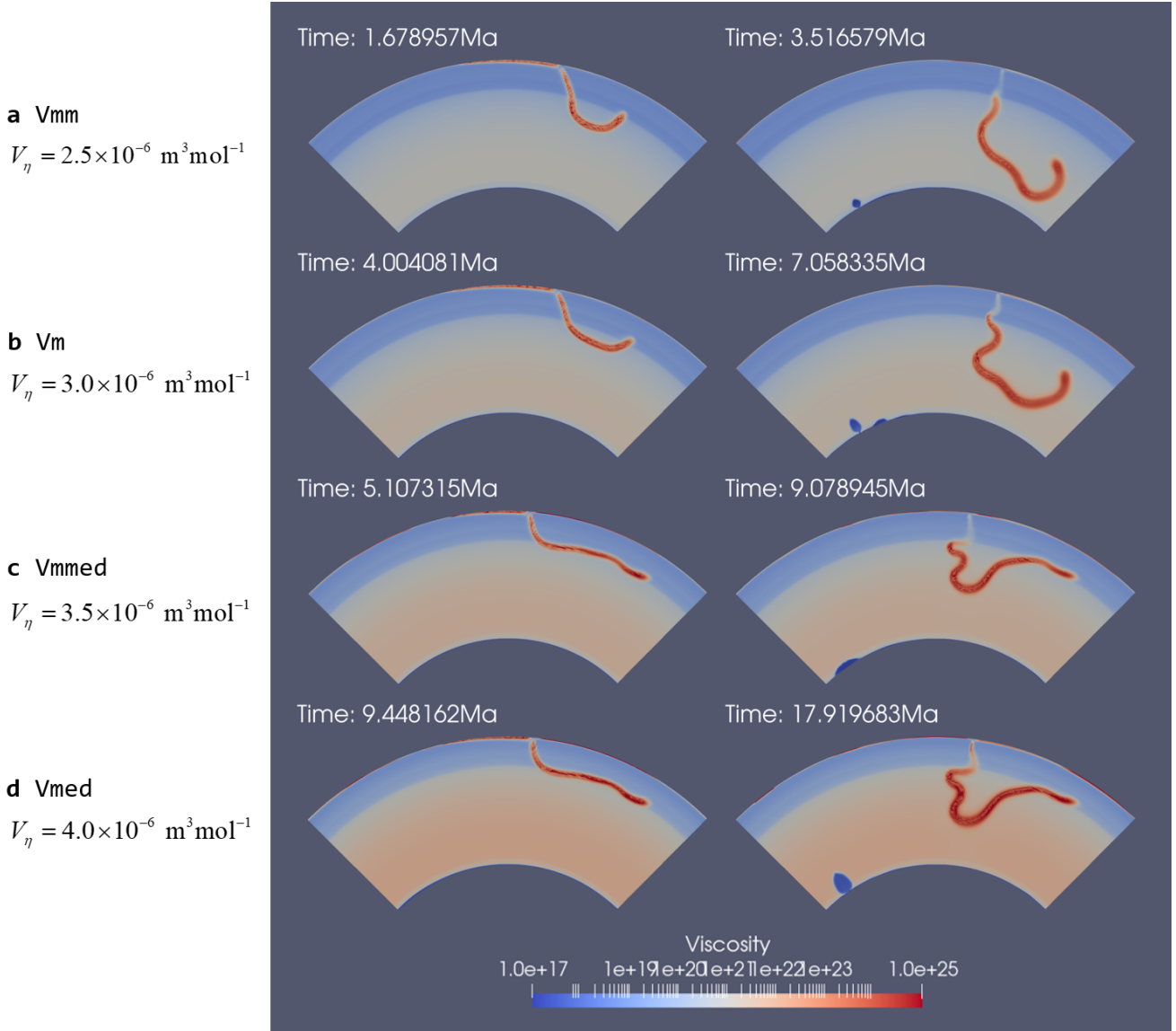


Figure 9: Snapshots of viscosity fields for models with different  $V_\eta^{\text{UM}}$ .

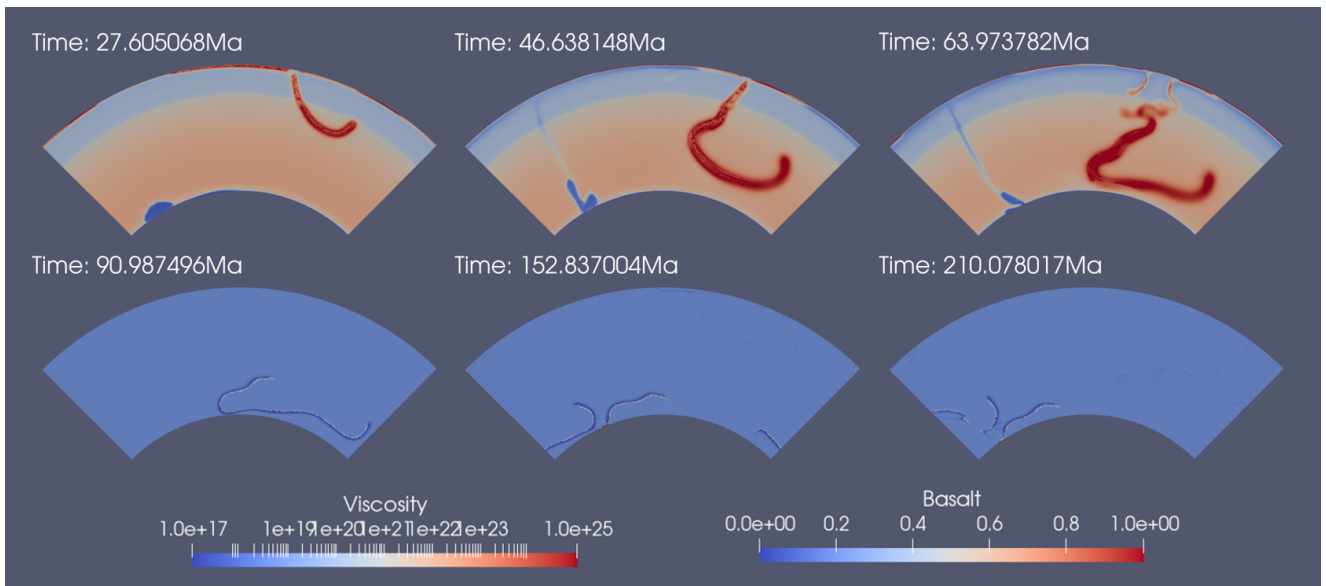


Figure 10: Evolution of model VmE0p. The upper panel shows viscosity fields for early stages, and the lower panel shows composition fields for later stages.

$VmEOP$  reproduces the slab with almost exactly the same bowl shape, even when  $\eta_0$  is adjusted to compensate for lower viscosity.

### 3.3 Influence of Clapeyron slope

For a specific phase change, Clapeyron slope is defined as the tangential slope of the coexistence curve on a P-T diagram:

$$\gamma = \frac{dP}{dT} \quad (12)$$

During model simulation, the penetration phase has been identified as the phase that modifies most the geometry of the slab. The Clapeyron slope of the 660km phase transition hence also plays an important role in subduction dynamics and slab morphology. At the lower boundary of MTZ, Ringwoodite and Majorite transition to perovskite phase into Bridgmanite (Ishii, Huang, et al. 2018). This phase transition is associated with a positive density jump, but a negative Clapeyron slope (Ishii, Kojitani, and Akaogi 2011). Therefore, colder material crossing the 660 phase transition from above experiences positive buoyancy compared to its surroundings, which resists penetration.

In model STD, a Clapeyron slope of  $-2.5 \text{ MPa K}^{-1}$  is used, and penetration indeed faces strong resistance at the 660-discontinuity. It is shown by varying viscosity jump (section 3.2.1) that different  $\Delta\eta_{660}$  produce similar dynamics and cannot account for the resistance. Instead, by varying the 660km Clapeyron slope (fig.11), it can be further shown that the negative Clapeyron slope is the main source of this resistance.

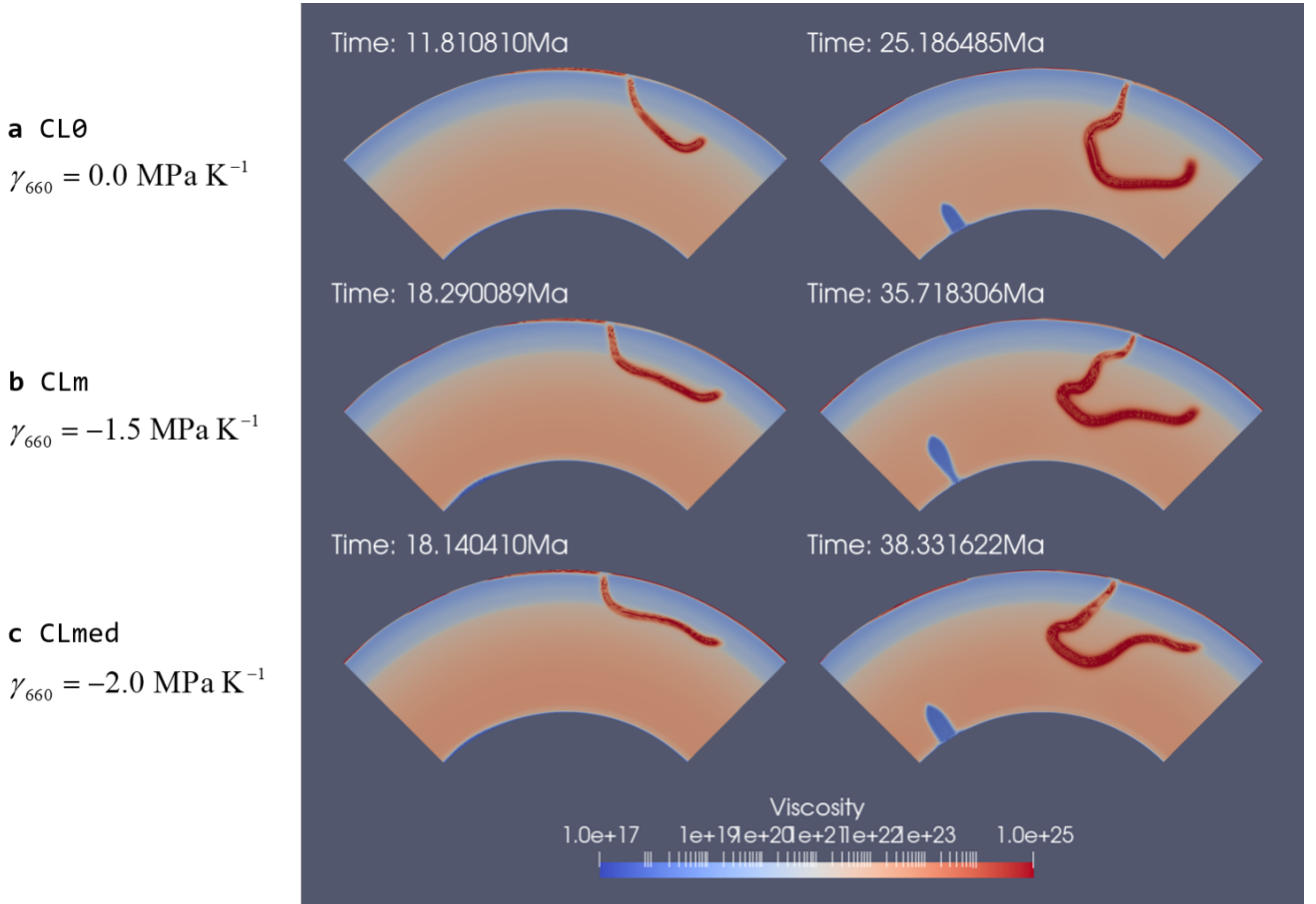


Figure 11: Snapshots of viscosity fields for models with different  $\gamma_{660}$ . Each row shows evolution of one model.

Models with reduced 660 phase transition Clapeyron slope (models CL0, CLm, fig.11) show simultaneous deflection and penetration. As a result, the slab at the end of penetration phase also takes the shape of a bowl (model CL0, fig.11-a, 25.2Myr snapshot), or some geometry between bowl-shape and dipper-shape (model CLm, fig.11-b, 35.7Myr snapshot). Similar features are also observed in low upper-mantle  $V_\eta$  cases (e.g. model  $Vm$ , fig.9-b, 7Myr), also as a result of simultaneous deflection and penetration.

Compared to other models with similar level of lower-mantle viscosity, lowering the absolute value of the Clapeyron slope expectedly accelerates the penetration process by 10 – 20Myr (48Myr to 26 – 38Myr, fig.11). This further verifies the resistance effect of negative Clapeyron slope.

Compared to low  $V_\eta$  models, despite similar morphology, the slabs tend to be more inclined in the lower mantle, and no "horizontal" bottom is observed when they approach CMB. The explanation for this difference is yet to be confirmed, but we argue that it might be caused by stronger push from the later subducted material. This argument is supported by: i) a higher upper-mantle radial viscosity gradient, and ii) more steady trench location, as observed from simulations.

### 3.4 Influence of plate strength

On the other side of the slab-mantle interaction, plate strength also plays an important role in subduction dynamics and slab geometry. Given diffusion creep rheology in this model, plate strength is only dependent on three factors: i) pressure, ii) temperature, and iii) brittle/ductile yield strength.

Among the 3 factors, pressure cannot produce significant lateral heterogeneity in viscosity, as it is mainly correlated with depth, and dynamic pressure is often much smaller than hydrostatic pressure. The effect of initial temperature profile is discussed in section 3.4.1, and the effect of yield strength in section 3.4.2.

#### 3.4.1 Plate age

In absence of imposed surface velocity field, plate velocity or special initiation structure, temperature anomaly in the plate is the main contributor to the negative buoyancy which initiates the subduction. The initial temperature profile, as discussed in section 2.3.1, is controlled by age distribution of the slab, which is in turn determined by spreading velocity. Here the spreading velocity is varied between 1 and 4 cm yr<sup>-1</sup> (fig. 12). This corresponds to an age of 500Myr to 125Myr at the right edge of the plate, where subduction initiates.

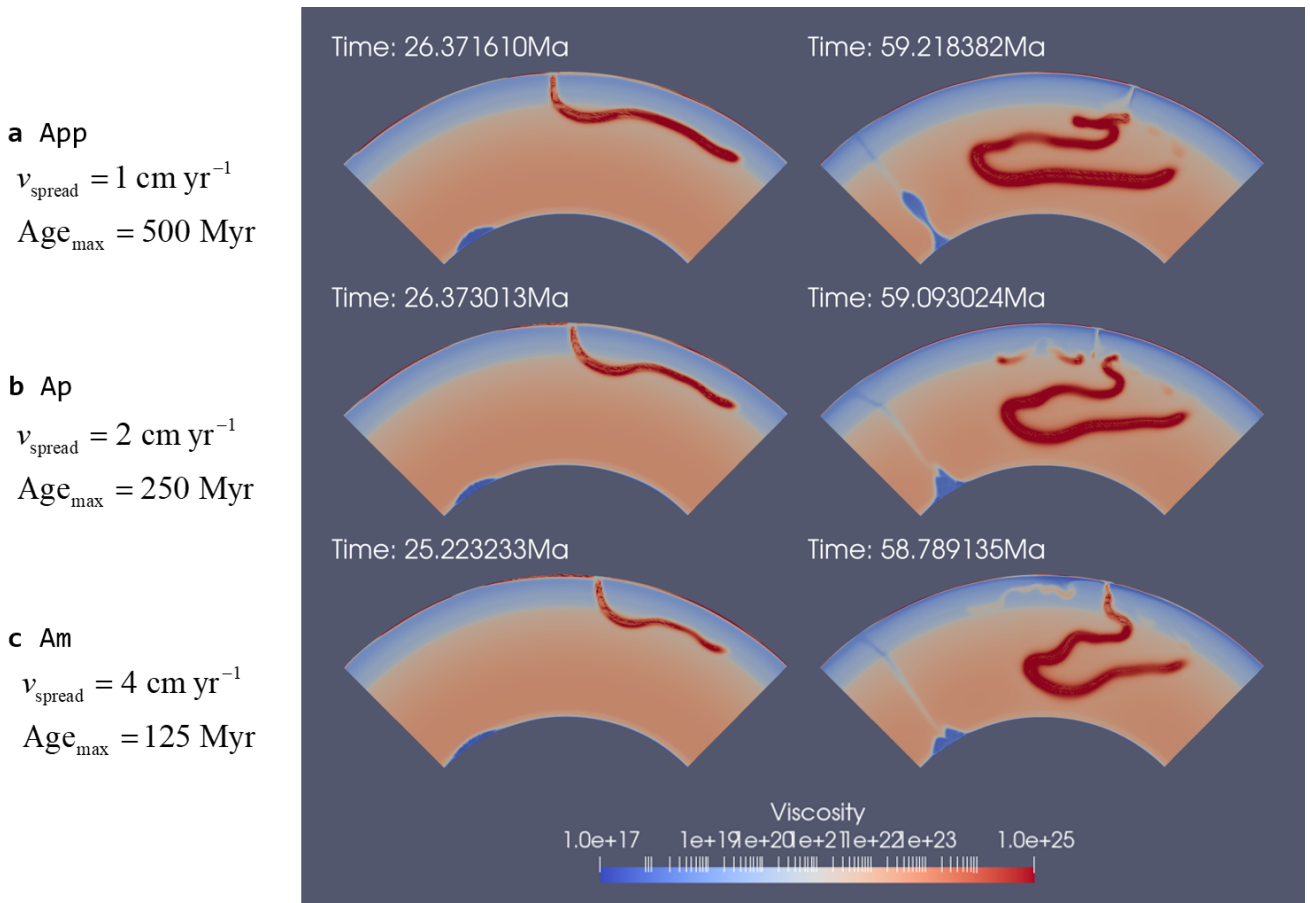


Figure 12: Snapshots of viscosity fields for models with different ages. Each row shows evolution of one model.

Models within this reasonable range shows no significant difference in subduction or penetration dynamics. Key features are already summarized in section 3.1. Older and colder slabs gain more negative buoyancy, accelerating subduction. Hence more material is accumulated above the 660-discontinuity for colder plates, and the lateral spreading is longer prior to penetration. Under similar modifications including bending and folding, the slabs obtain their dipper(model Am, fig.12-c)-to-hairpin(model App, fig.12-a) geometry as they enter the lower mantle.

Initial plate age and viscosity only seems to have very minor effects on the timeline of dynamics. While the amount of accumulated material before penetration varies and the slabs feature different lengths of bottom segment, the phases follow virtually the same timeline without significant advance or lag. This indicates that initial plate strength only affects initial subduction, and the later stages are controlled by mantle properties given the same rheology.

### 3.4.2 Plate yield strength

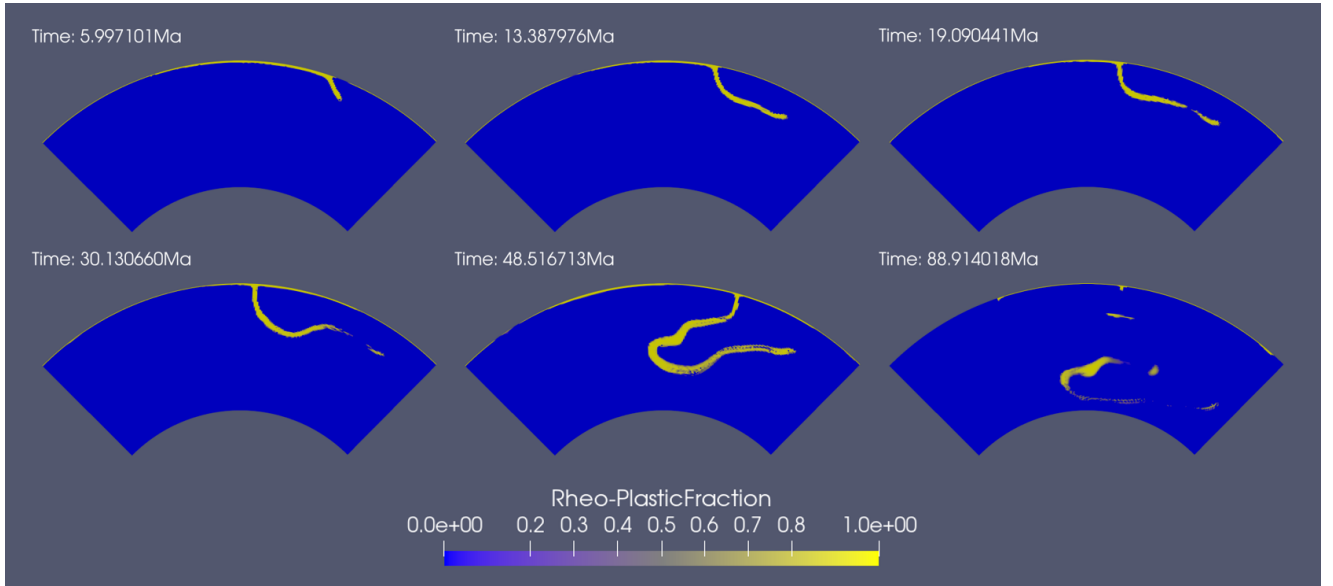


Figure 13: Snapshots of dominant rheology for model STD. Rheology is shown by visualizing an index indicating fraction of plastic yielding. Yielding is concentrated in plates, and diminishes for laterally lying segments (20–30Myr) and for slow-deforming slabs approaching CMB (89Myr).

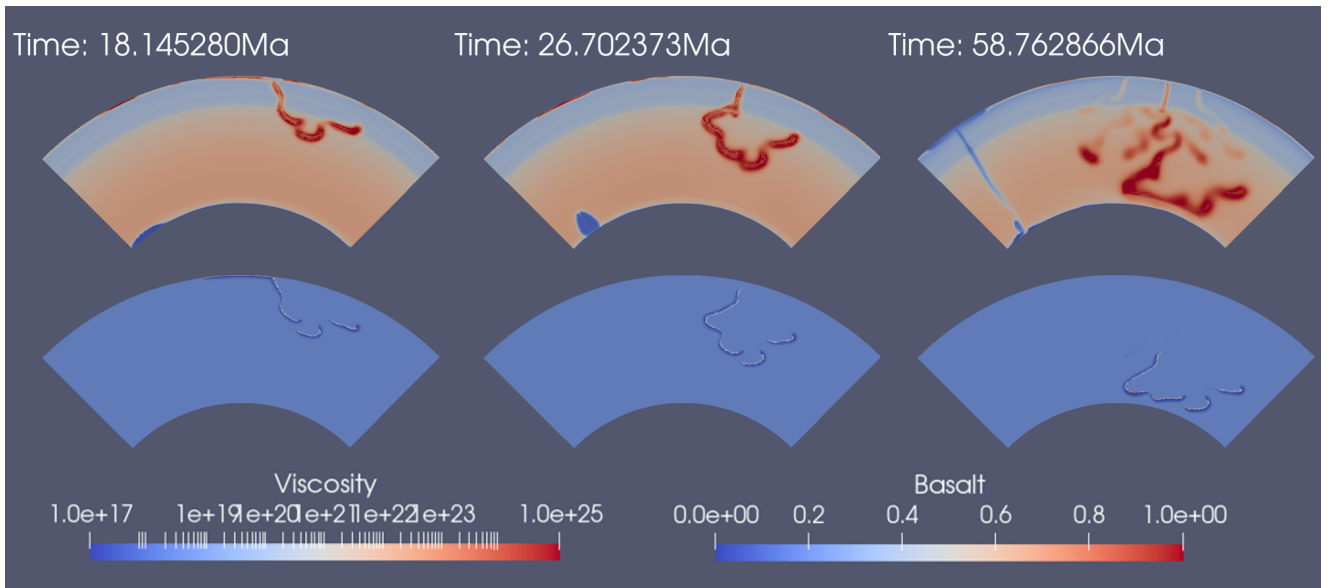


Figure 14: Snapshots of model ETAmE0pSYm. Upper panel and lower panel show the same fields as fig.3

Two kinds of yielding (section 3.4.2) are implemented in the model, and despite different mechanisms, both provide an upper bound of viscosity given certain deformation rate in a similar manner. Material cannot resist the high stress caused by rapid deformation (high  $\dot{\epsilon}$ ); it yields or breaks in response to the velocity field. Yielding is particularly important at the early stages of subduction, when the static plate is dragged into motion by its negative buoyancy (fig.13).

A high yield strength ( $\sigma_{Y,0} = 20 \times 10^6 \text{ MPa}$ ) is used for ductile yielding for reference models. Models with yield strength an order of magnitude lower (VmE0pSYm, fig.14, and ETAmE0pSYm) are simulated to study its effect. The main characteristic arising from lower yield strength is segmentation at early subduction, due to the plate's reaching yield strength at an early stage, and differentiating into segments as the yield strength cannot maintain the plate as a whole. In general, lower yield strength facilitates curving of the slab, producing more complex morphology. For instance, bowl-shaped morphology after penetration is replaced by broccoli-shaped morphology for low  $V_\eta$  cases (fig.14).

Yield strength does not change the general dynamics of different phases, as the overall slab geometry and phase timelines are all similar.

## 4 Discussions

### 4.1 Regimes for spreading and penetration

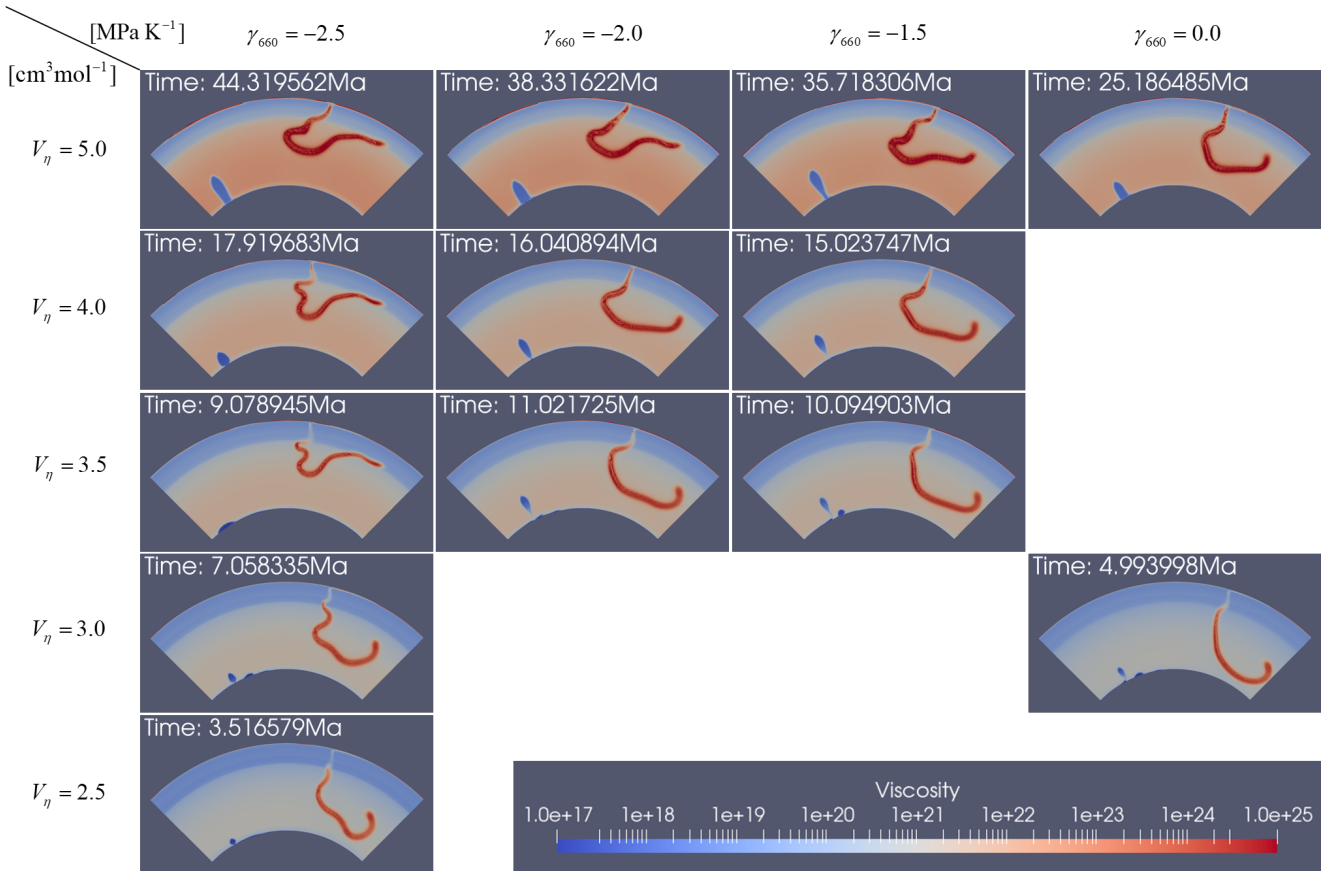


Figure 15: Distribution of slab morphology at the end of phase II in the  $\gamma_{660} - V_\eta^{\text{UM}}$  parameter space

In this study, two parameters are able to produce different dynamic regimes as they vary within their respective ranges, namely upper-mantle activation volume  $V_\eta$ , and 660 Clapeyron slope  $\gamma_{660}$ . Other parameters, including viscosity jump  $\Delta\eta_{660}$ , plate age, and plate yield strength, seem to produce only quantitative change in subduction dynamics or overall slab geometries, at least within the reasonable range examined here.

The qualitative difference between two regimes observed here can be summarized as whether lateral spreading and penetration process occupy two distinct time periods. In one group of models including the STD model, the slab develops large lateral extent before the latter part finally penetrates the 660. This regime is hereafter referred to as strong-spreading regime. Alternatively, with either  $V_\eta$  or  $\gamma_{660}$  lower than certain threshold,

penetration of the 660 blends in with lateral spreading of the slab, and the distinction between phase I and phase II is blurred. With penetrating process occurring at the same time with subduction and lateral spreading, the slab sinks down into the lower mantle faster as a whole and develops different geometries. This latter regime is hereafter referred to as strong-penetration regime.

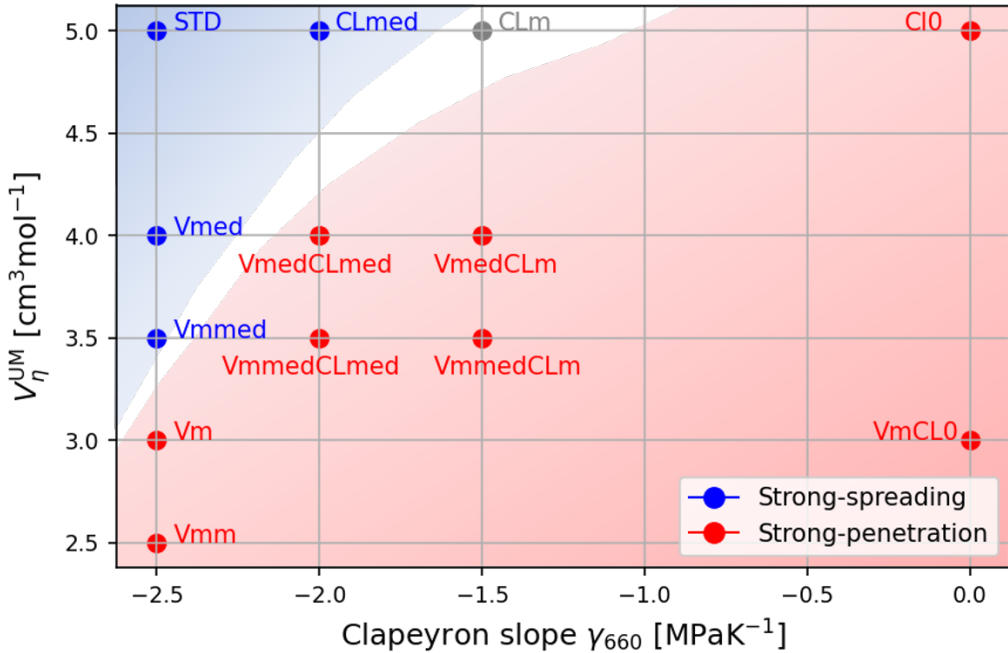


Figure 16: Regime plot for spreading-penetration regimes in the  $\gamma_{660} - V_\eta^{\text{UM}}$  parameter space. The models are the same as in fig.15

Supplemented by additional model runs, the geometries of slabs at the end of phase II are collected (fig.15). Identification of different regimes is based on i) dynamics timeline, whether lateral spreading dynamics lasts for a considerable time before penetration, and ii) slab morphology, whether the slab features considerable concave curvature at the bottom, which should result from differential sinking of the rear and the front part. According to these criteria, almost all models present have clear-cut regimes to assign to, except for ambiguity in model CLm. Based on the identified regimes, a regime diagram is produced (fig.16). Tradeoff between  $V_\eta$  and  $\gamma_{660}$  is readily observed in the sense of their effect on the spreading-penetration regime. The transition between the two regimes lies somewhere between models Vmmed-CLmed, and models Vm-VmmedCLmed-VmedCLm-CL0.

## 4.2 Compositional segregation and accumulation

The relevance of slab morphology as it enters the lower mantle (end of phase II) to dynamics near CMB and compositional segregation is discussed in this section. In most models, a flat horizontal slab bottom is identified when subducted slab approaches CMB. This either comes from the bottom in bowl-shaped slab morphology, or from the flattened handle of the dipper-shaped slab morphology, and is therefore a robust feature regardless of spreading-penetration regime. A small dome sometimes forms as the slab lies down on CMB (see fig.8), particularly in strong-spreading cases, as is also observed by P. J. Tackley 2011.

A quantitative approach is taken to examine the composition buildup at CMB. We take the mean composition at the lowermost 150km of the domain weighted by the cell volumes, as the mean composition near CMB at a given snapshot. Segregation first happens at junction points with significant curvature; the thinning of the slab at these points breaks the slab into multiple segments. Note that as the slab approaches CMB, the horizontal bottom always keeps the original order of compositional layering, i.e. denser basalt on top and lighter harzburgite beneath. This gives the first-arriving negative peak that shows up in all models (fig.17, 18). The segments from the bottom slab are hence mechanically unstable, and tend to reorient vertically under plume perturbations and their own gravitational torque. At the same time, compositional segregation precipitates basalt onto CMB, giving a mean composition value greater than the background value, which is

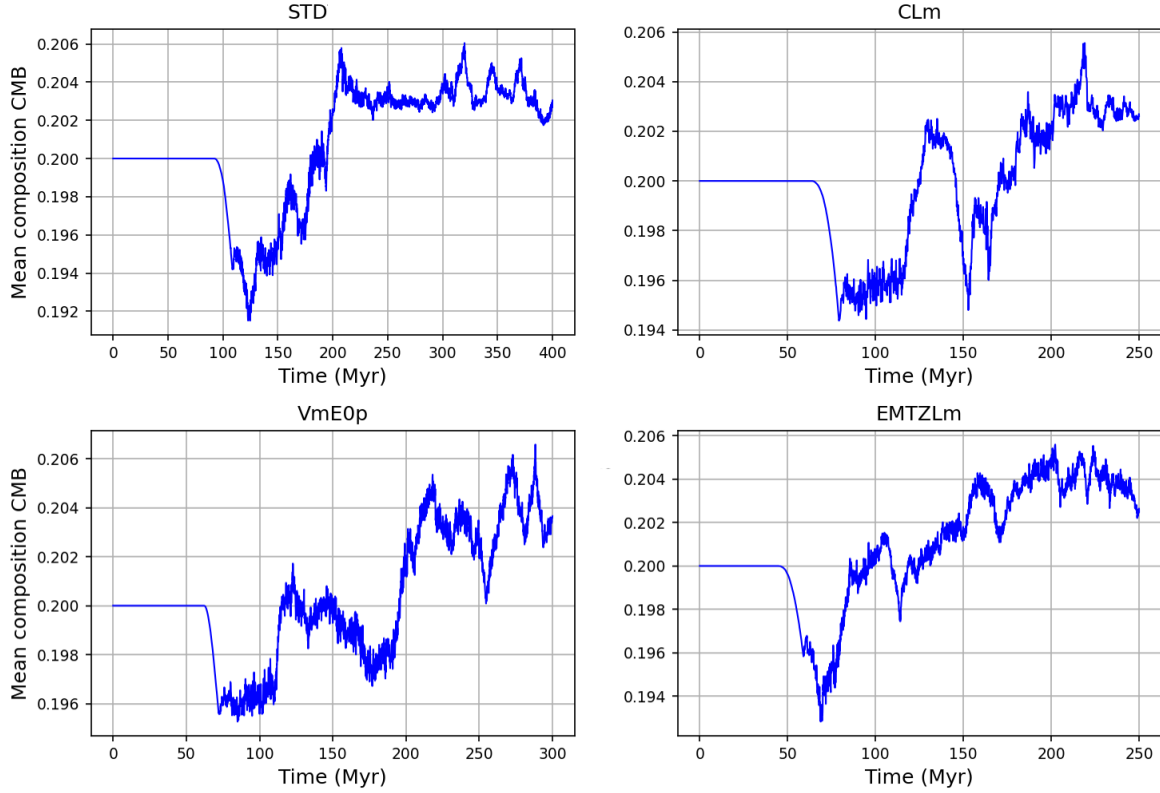


Figure 17: Basalt buildup at CMB for representative models

observed in most models (fig.17).

Recycling of the subducted material is ubiquitous in all models, and the preservation of such heterogeneity is an issue. One interesting observation is that in multiple cases, segregation does not occur at CMB; the entire slab segments, which have settled down at CMB, may be partially recycled and rise again to  $200 \sim 400$ km above the CMB, as if living deads are summoned from their tombs. In a majority of cases the enrichment of basalt can be preserved at least for 100Myr (fig.17), until at least 200Myr after the slab reaches CMB. In some cases (fig.18), however, a decline in basalt is observed after only 50Myr of enrichment, and the composition drops back to its background value.

In this study, we are unable to distinguish the parameters that control such different behaviours. Further work may be necessary to identify such parameters.

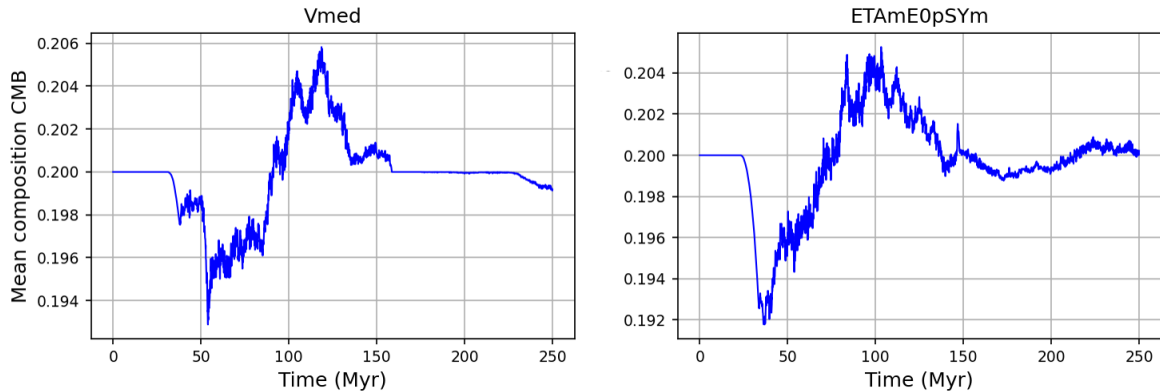


Figure 18: Models that show unstable preservation of basalt

### 4.3 Assumptions, justifications and limitations

Final models are always compromise between model accuracy and realism, and computational cost. Assumptions have been made at the cost of switching off certain behaviours which may lower the credibility of the models, so as to enable systematic study of some variables. Some assumptions are justified by either analyzing the behaviour, or extra model runs which does not require certain assumptions.

All aforementioned models assume a free-slip boundary condition at the surface. A free-surface boundary condition with no surface traction is more realistic and ideal, but cannot be readily applied in finite difference/finite volume codes. Instead, a sticky air layer or a realistic air layer needs to be imposed at the top of the domain to implement a free surface. This often lowers the efficiency of the code, as induced velocity field in the air layer compresses available time steps satisfying stability criterion. Both free-slip and free-surface boundary conditions have been used in previous geodynamic studies (for free-surface, e.g. Garel et al. 2014, Grima, Lithgow-Bertelloni, and Crameri 2020; for free-slip, e.g. Stegman et al. 2010) and yield reasonable results. In our case, usage of free-slip boundary condition is further justified by a model run (model FSDuretz, fig.A2) which utilizes free surface implementation described by Duretz, May, and Yamato 2016. At additional computational expense, geometry of the slab as it enters the lower mantle is quite similar, despite some extra yielding during penetration which shortens the viscous tail of the slab. Hence, the slab geometry developed under free-slip surface boundary condition should be representative of the case in reality.

Absence of melt generation is another shortcoming of the models. On present-day Earth melt can be continuously generated at spreading centres or subduction zones, providing further material available for subduction. In the aforementioned models melt is ignored, and only initial slab is compositionally distinct from the mantle. A supplementary model with basaltic melt generation is introduced (model MELT, fig.A3), where melt is generated when temperature of tracers exceeds basalt solidus, and shallow melts are transported to the surface to account for eruption. This simulation shows subsequent melt production does not affect first-subducted slab, as the dynamics and the morphology virtually remain unchanged, except for subsequent littering by newly produced basalt at scattered locations. The credibility of the first-subducted slab dynamics and morphology presented above is thus partially justified. However, it should be noted that in model MELT, the position of later-stage basalt production is constantly shifting, and a desired initial-slab-like unilateral decreasing temperature profile cannot be obtained. Therefore, the later-stage melts only appear as scattered, 2-sided downwellings, instead of stable, one-sided subduction, and its relevance to real Earth is doubted.

The mantle rheology applied here assumes grain-size-independent diffusion creep. As the description suggests, two ingredients, grain size evolution, and dislocation creep, are neglected. It has been argued that dislocation creep is dominant in shallow upper mantle, but loses its dominance in the lower upper mantle (S.-i. Karato 1992). However, experiments also show dominance of dislocation creep under high pressure equivalent to lower upper mantle depth (L. Li et al. 2003, Mainprice et al. 2005). Therefore, this assumption is admittedly not justified, and may lead to limitations in this study. The role of dislocation creep and grain size evolution in shaping the slab morphology needs to be further studied.

## 5 Conclusion

Using a chemical-thermal-mechanical simulation code, we studied the effect of different parameters on morphology of the slab when it enters lower mantle. Results show that varying upper-mantle activation volume  $V_{\eta}^{\text{UM}}$  within  $[2.5 \times 10^{-6}, 5.0 \times 10^{-6}] \text{ m}^3 \text{ mol}^{-1}$  and 660 Clapeyron slope  $\gamma_{660}$  within  $[-2.5, 0.0] \text{ MPa K}^{-1}$  yields different dynamic regimes, referred to as strong-spreading regime and strong-penetration regime, resulting in dipper-shaped morphology and bowl-shaped morphology respectively. Other parameters, including 660 viscosity jump, plate age and slab yield strength do not seem to have such influence that induce qualitative changes.

Despite the difference in slab geometry, the dynamics near the CMB and compositional segregation follows the same pattern. The slab usually features a quasi-horizontal bottom as it approaches CMB, which is segmented into multiple parts due to segregation and thinning at certain locations. Vertical orientation of subducted slab segments is often observed at later stages. Compositional segregation is accompanied by precipitation of basalt onto CMB and recycling of the material back into the mantle at the same time. The basalt accumulation at CMB is almost always observed, but preservation of enrichment of basalt near CMB is

varied, ranging from less than 50Myr to over 200Myr. The basalt preservation does not seem to have simple relation with the slab morphology at the end of phase II, and further research is required to determine the controlling parameters.

## References

- Christensen, Ulrich R. and Albrecht W. Hofmann (1994). "Segregation of subducted oceanic crust in the convecting mantle". In: *Journal of Geophysical Research: Solid Earth* 99.B10, pp. 19867–19884. DOI: <https://doi.org/10.1029/93JB03403>. eprint: <https://agupubs.onlinelibrary.wiley.com/doi/pdf/10.1029/93JB03403>. URL: <https://agupubs.onlinelibrary.wiley.com/doi/abs/10.1029/93JB03403>.
- Duretz, T., D.A. May, and P. Yamato (Jan. 2016). "A free surface capturing discretization for the staggered grid finite difference scheme". In: *Geophysical Journal International* 204.3, pp. 1518–1530. ISSN: 0956-540X. DOI: [10.1093/gji/ggv526](https://doi.org/10.1093/gji/ggv526). eprint: <https://academic.oup.com/gji/article-pdf/204/3/1518/17368851/ggv526.pdf>. URL: <https://doi.org/10.1093/gji/ggv526>.
- Dziewonski, Adam M., Vedran Lekic, and Barbara A. Romanowicz (2010). "Mantle Anchor Structure: An argument for bottom up tectonics". In: *Earth and Planetary Science Letters* 299.1, pp. 69–79. ISSN: 0012-821X. DOI: <https://doi.org/10.1016/j.epsl.2010.08.013>. URL: <https://www.sciencedirect.com/science/article/pii/S0012821X10005236>.
- Forsyth, Donald and Seiya Uyeda (Oct. 1975). "On the Relative Importance of the Driving Forces of Plate Motion". In: *Geophysical Journal International* 43.1, pp. 163–200. ISSN: 0956-540X. DOI: [10.1111/j.1365-246X.1975.tb00631.x](https://doi.org/10.1111/j.1365-246X.1975.tb00631.x). eprint: <https://academic.oup.com/gji/article-pdf/43/1/163/1576393/43-1-163.pdf>. URL: <https://doi.org/10.1111/j.1365-246X.1975.tb00631.x>.
- Fukao, Yoshio et al. (1992). "Subducting slabs stagnant in the mantle transition zone". In: *Journal of Geophysical Research: Solid Earth* 97.B4, pp. 4809–4822. DOI: <https://doi.org/10.1029/91JB02749>. eprint: <https://agupubs.onlinelibrary.wiley.com/doi/pdf/10.1029/91JB02749>. URL: <https://agupubs.onlinelibrary.wiley.com/doi/abs/10.1029/91JB02749>.
- Garel, F. et al. (2014). "Interaction of subducted slabs with the mantle transition-zone: A regime diagram from 2-D thermo-mechanical models with a mobile trench and an overriding plate". In: *Geochemistry, Geophysics, Geosystems* 15.5, pp. 1739–1765. DOI: <https://doi.org/10.1002/2014GC005257>. eprint: <https://agupubs.onlinelibrary.wiley.com/doi/pdf/10.1002/2014GC005257>. URL: <https://agupubs.onlinelibrary.wiley.com/doi/abs/10.1002/2014GC005257>.
- Garnero, Edward J. and Allen K. McNamara (2008). "Structure and Dynamics of Earth's Lower Mantle". In: *Science* 320.5876, pp. 626–628. ISSN: 0036-8075. DOI: [10.1126/science.1148028](https://doi.org/10.1126/science.1148028). eprint: <https://science.sciencemag.org/content/320/5876/626.full.pdf>. URL: <https://science.sciencemag.org/content/320/5876/626>.
- Grima, Antoniette Greta, Carolina Lithgow-Bertelloni, and Fabio Crameri (2020). "Orphaning Regimes: The Missing Link Between Flattened and Penetrating Slab Morphologies". In: *Frontiers in Earth Science* 8, p. 374. ISSN: 2296-6463. DOI: [10.3389/feart.2020.00374](https://doi.org/10.3389/feart.2020.00374). URL: <https://www.frontiersin.org/article/10.3389/feart.2020.00374>.
- Herzberg, C. et al. (2007). "Temperatures in ambient mantle and plumes: Constraints from basalts, picroites, and komatiites". In: *Geochemistry, Geophysics, Geosystems* 8.2. DOI: <https://doi.org/10.1029/2006GC001390>. eprint: <https://agupubs.onlinelibrary.wiley.com/doi/pdf/10.1029/2006GC001390>. URL: <https://agupubs.onlinelibrary.wiley.com/doi/abs/10.1029/2006GC001390>.
- Hirth, Greg and David Kohlstedt (2004). "Rheology of the Upper Mantle and the Mantle Wedge: A View from the Experimentalists". In: *Inside the Subduction Factory*. American Geophysical Union (AGU), pp. 83–105. ISBN: 9781118668573. DOI: [10.1029/138GM06](https://doi.org/10.1029/138GM06). eprint: <https://agupubs.onlinelibrary.wiley.com/doi/pdf/10.1029/138GM06>. URL: <https://agupubs.onlinelibrary.wiley.com/doi/abs/10.1029/138GM06>.
- Ishii, Takayuki, Rong Huang, et al. (2018). "Complete agreement of the post-spinel transition with the 660-km seismic discontinuity". In: *Scientific Reports* 8.1. URL: <https://doi.org/10.1038/s41598-018-24832-y>.
- Ishii, Takayuki, Hiroshi Kojitani, and Masaki Akaogi (2011). "Post-spinel transitions in pyrolite and Mg<sub>2</sub>SiO<sub>4</sub> and akimotoite-perovskite transition in MgSiO<sub>3</sub>: Precise comparison by high-pressure high-temperature experiments with multi-sample cell technique". In: *Earth and Planetary Science Letters* 309.3, pp. 185–197. ISSN: 0012-821X. DOI: [10.1016/j.epsl.2011.06.023](https://doi.org/10.1016/j.epsl.2011.06.023). URL: <https://www.sciencedirect.com/science/article/pii/S0012821X11003943>.

- Karato, Shun-ichiro (1992). "On the Lehmann discontinuity". In: *Geophysical Research Letters* 19.22, pp. 2255–2258. DOI: <https://doi.org/10.1029/92GL02603>. eprint: <https://agupubs.onlinelibrary.wiley.com/doi/pdf/10.1029/92GL02603>. URL: <https://agupubs.onlinelibrary.wiley.com/doi/abs/10.1029/92GL02603>.
- Korenaga, Jun and Shun-Ichiro Karato (2008). "A new analysis of experimental data on olivine rheology". In: *Journal of Geophysical Research: Solid Earth* 113.B2. DOI: [10.1029/2007JB005100](https://doi.org/10.1029/2007JB005100). eprint: <https://agupubs.onlinelibrary.wiley.com/doi/pdf/10.1029/2007JB005100>. URL: <https://agupubs.onlinelibrary.wiley.com/doi/abs/10.1029/2007JB005100>.
- Li, Chang et al. (2008). "A new global model for P wave speed variations in Earth's mantle". In: *Geochemistry, Geophysics, Geosystems* 9.5. DOI: <https://doi.org/10.1029/2007GC001806>. eprint: <https://agupubs.onlinelibrary.wiley.com/doi/pdf/10.1029/2007GC001806>. URL: <https://agupubs.onlinelibrary.wiley.com/doi/abs/10.1029/2007GC001806>.
- Li, Li et al. (2003). "Olivine flow mechanisms at 8 GPa". In: *Physics of the Earth and Planetary Interiors* 138.2, pp. 113–129. ISSN: 0031-9201. DOI: [https://doi.org/10.1016/S0031-9201\(03\)00065-7](https://doi.org/10.1016/S0031-9201(03)00065-7). URL: <https://www.sciencedirect.com/science/article/pii/S0031920103000657>.
- Mainprice, David et al. (2005). "Pressure sensitivity of olivine slip systems and seismic anisotropy of Earth's upper mantle". In: *Nature* 433, pp. 731–733. DOI: [10.1038/nature03266](https://doi.org/10.1038/nature03266). URL: <https://doi.org/10.1038/nature03266>.
- Stegman, D.R. et al. (2010). "A regime diagram for subduction styles from 3-D numerical models of free subduction". In: *Tectonophysics* 483.1. Convergent plate margin dynamics: New perspectives from structural geology, geophysics and geodynamic modelling, pp. 29–45. ISSN: 0040-1951. DOI: <https://doi.org/10.1016/j.tecto.2009.08.041>. URL: <https://www.sciencedirect.com/science/article/pii/S0040195109004776>.
- Tackley, P.J. et al. (2013). "Mantle dynamics in super-Earths: Post-perovskite rheology and self-regulation of viscosity". In: *Icarus* 225.1, pp. 50–61. ISSN: 0019-1035. DOI: <https://doi.org/10.1016/j.icarus.2013.03.013>. URL: <https://www.sciencedirect.com/science/article/pii/S0019103513001231>.
- Tackley, Paul J. (2008). "Modelling compressible mantle convection with large viscosity contrasts in a three-dimensional spherical shell using the yin-yang grid". In: *Physics of the Earth and Planetary Interiors* 171.1. Recent Advances in Computational Geodynamics: Theory, Numerics and Applications, pp. 7–18. ISSN: 0031-9201. DOI: <https://doi.org/10.1016/j.pepi.2008.08.005>. URL: <https://www.sciencedirect.com/science/article/pii/S0031920108002276>.
- Tackley, Paul J. (2011). "Living dead slabs in 3-D: The dynamics of compositionally-stratified slabs entering a "slab graveyard" above the core-mantle boundary". In: *Physics of the Earth and Planetary Interiors* 188.3. Proceedings of the 12th Symposium of SEDI, pp. 150–162. ISSN: 0031-9201. DOI: <https://doi.org/10.1016/j.pepi.2011.04.013>. URL: <https://www.sciencedirect.com/science/article/pii/S003192011100077X>.
- Wolstencroft, M. and J. H. Davies (2011). "Influence of the Ringwoodite-Perovskite transition on mantle convection in spherical geometry as a function of Clapeyron slope and Rayleigh number". In: *Solid Earth* 2, pp. 315–326. DOI: [10.5194/se-2-315-2011](https://doi.org/10.5194/se-2-315-2011). URL: <https://se.copernicus.org/articles/2/315/2011/se-2-315-2011.pdf>.
- Yan, Jun, Maxim D. Ballmer, and Paul J. Tackley (2020). "The evolution and distribution of recycled oceanic crust in the Earth's mantle: Insight from geodynamic models". In: *Earth and Planetary Science Letters* 537, p. 116171. ISSN: 0012-821X. DOI: <https://doi.org/10.1016/j.epsl.2020.116171>. URL: <https://www.sciencedirect.com/science/article/pii/S0012821X2030114X>.

## A Appendix: supplementary models and plots

Table A1: List of all models presented in the paper

| Model name  | $\Delta\eta_{660}$<br>[-] | $\gamma_{660}$<br>[MPa K $^{-1}$ ] | $V_\eta^{\text{UM}}$<br>[cm $^3$ mol $^{-1}$ ] | $\eta_0$<br>[Pa · s] | $v_{\text{spread}}$<br>[cm yr $^{-1}$ ] | $\sigma_{Y,0}$<br>[MPa] |
|-------------|---------------------------|------------------------------------|--|----------------------|---|-------------------------|
| STD         | 3.0                       | -2.5                               | 5.0  | $10^{19}$            | 3.0                                     | 20                      |
| CLmed       | 3.0                       | -2.0                               | 5.0  | $10^{19}$            | 3.0                                     | 20                      |
| CLm         | 3.0                       | -1.5                               | 5.0  | $10^{19}$            | 3.0                                     | 20                      |
| CLO         | 3.0                       | 0.0                                | 5.0  | $10^{19}$            | 3.0                                     | 20                      |
| Vmed        | 3.0                       | -2.5                               | 4.0  | $10^{19}$            | 3.0                                     | 20                      |
| Vmmmed      | 3.0                       | -2.5                               | 3.5  | $10^{19}$            | 3.0                                     | 20                      |
| Vm          | 3.0                       | -2.5                               | 3.0  | $10^{19}$            | 3.0                                     | 20                      |
| Vmm         | 3.0                       | -2.5                               | 2.5  | $10^{19}$            | 3.0                                     | 20                      |
| VmedCLmed   | 3.0                       | -2.0                               | 4.0  | $10^{19}$            | 3.0                                     | 20                      |
| VmedCLm     | 3.0                       | -1.5                               | 4.0  | $10^{19}$            | 3.0                                     | 20                      |
| VmmmedCLmed | 3.0                       | -2.0                               | 3.5  | $10^{19}$            | 3.0                                     | 20                      |
| VmmmedCLm   | 3.0                       | -1.5                               | 3.5  | $10^{19}$            | 3.0                                     | 20                      |
| VmCLO       | 3.0                       | 0.0                                | 3.0  | $10^{19}$            | 3.0                                     | 20                      |
| App         | 3.0                       | 0.0                                | 3.0  | $10^{19}$            | 1.0                                     | 20                      |
| Ap          | 3.0                       | 0.0                                | 3.0  | $10^{19}$            | 2.0                                     | 20                      |
| Am          | 3.0                       | 0.0                                | 3.0  | $10^{19}$            | 4.0                                     | 20                      |
| EMTZLm      | 1.0                       | -2.5                               | 5.0  | $10^{19}$            | 3.0                                     | 20                      |
| EMTZLp      | 9.0                       | -2.5                               | 5.0  | $10^{19}$            | 3.0                                     | 20                      |
| VmEOp       | 9.0                       | -2.5                               | 3.0  | $10^{20}$            | 3.0                                     | 20                      |
| VmEOpSYm    | 9.0                       | -2.5                               | 3.0  | $10^{20}$            | 3.0                                     | 2.0                     |

Table A2: List of supplementary models

| Model name | Difference from STD  |
|------------|--|
| STDRESp    | uses a higher resolution (256 radial cells, 512 azimuthal cells) |
| FSDuretz   | uses a free-surface boundary condition                           |
| MELT       | includes basaltic melts  |

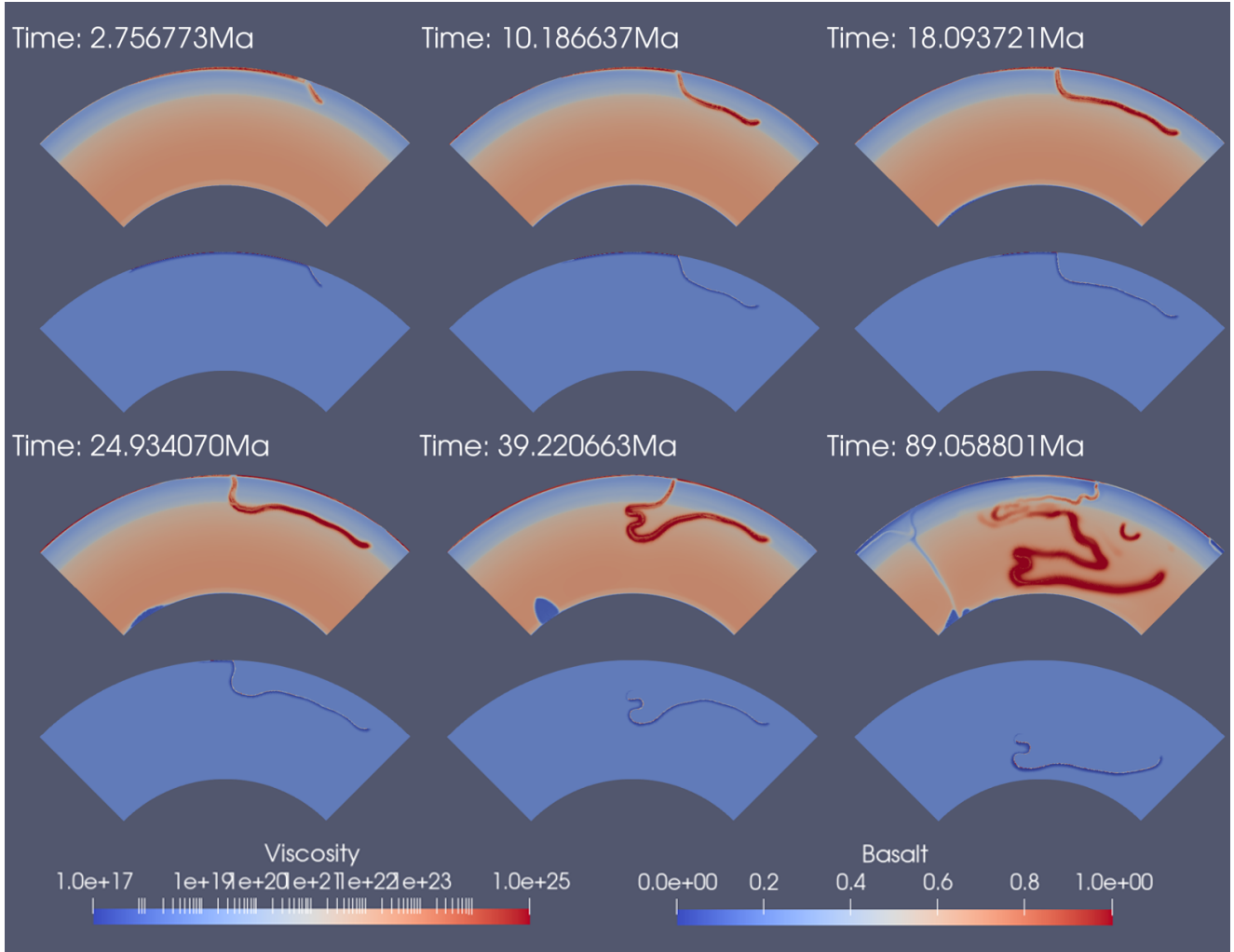


Figure A1: Evolution of high-resolution model STDRESp. For each time step, the viscosity field (upper plot in each frame) and the composition field (lower plot in each frame) are shown. Note that the overall morphology and dynamics are similar to that of model STD as in fig.3-5, and the timeline for different phases also remains unchanged.

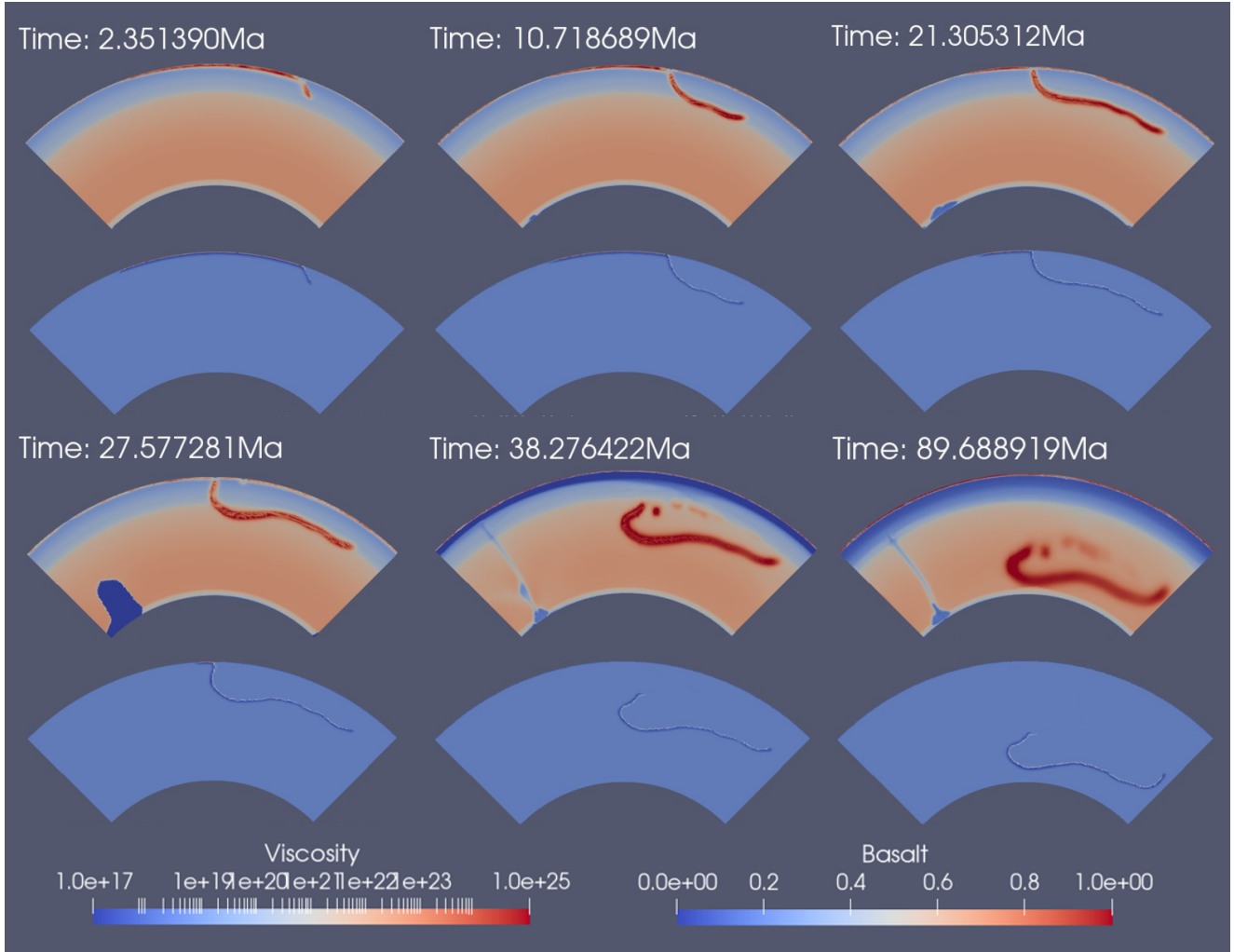


Figure A2: Evolution of free-surface model FSDuretz. For each time step, the viscosity field (upper plot in each frame) and the composition field (lower plot in each frame) are shown. Note that the overall morphology and dynamics are similar to that of model STD as in fig.3-5, except for absence of a viscous tail, and the timeline remains unchanged.

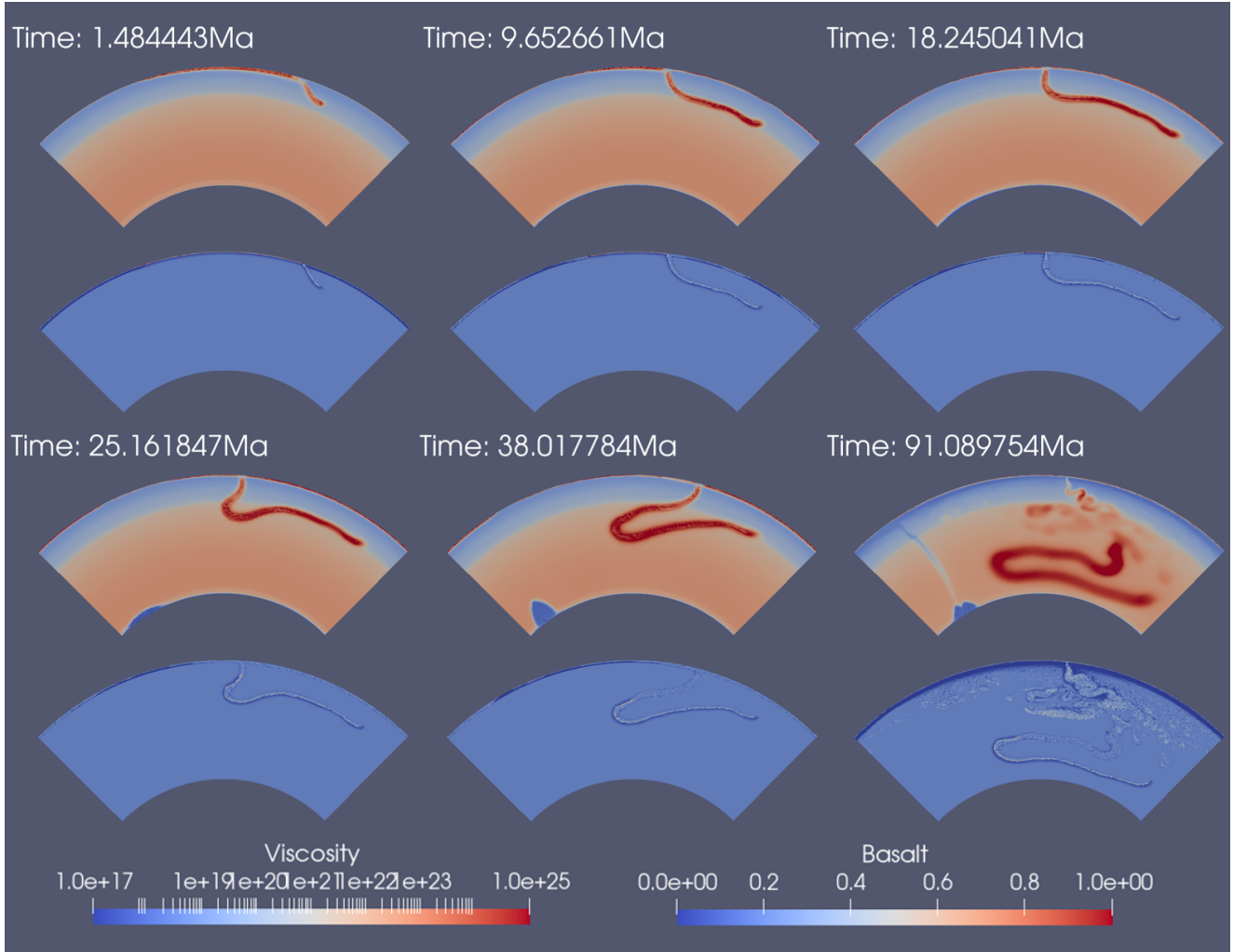


Figure A3: Evolution of model with basalt melt MELT. For each time step, the viscosity field (upper plot in each frame) and the composition field (lower plot in each frame) are shown. Note that the overall morphology and dynamics for the initial subduction are similar to that of model STD as in fig.3-5, and the timeline remains unchanged. The mantle is further littered with later downwelling, which follows different dynamics from the one-sided subducting initial slab.

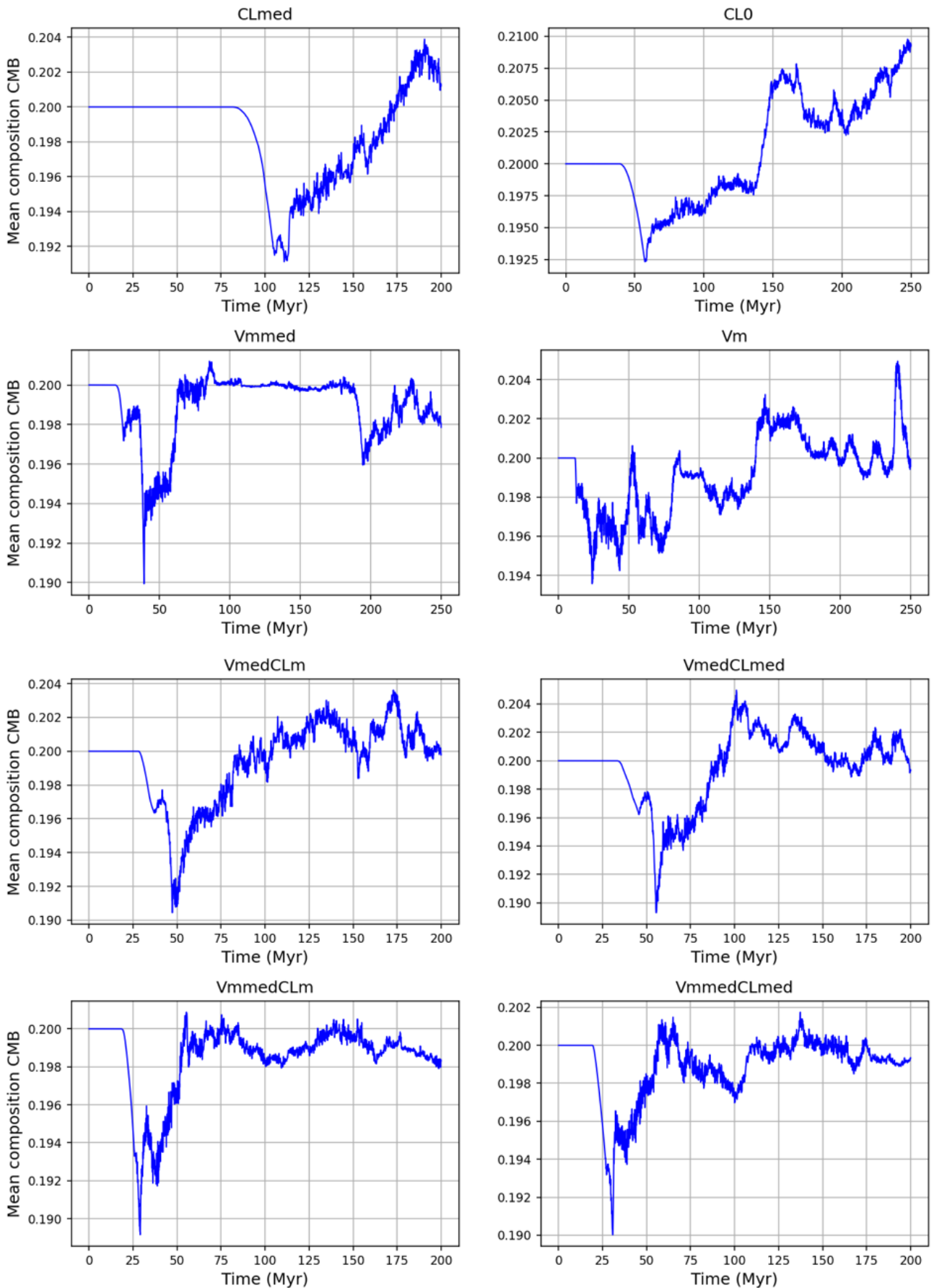


Figure A4: Evolution of basalt content near CMB for other models.

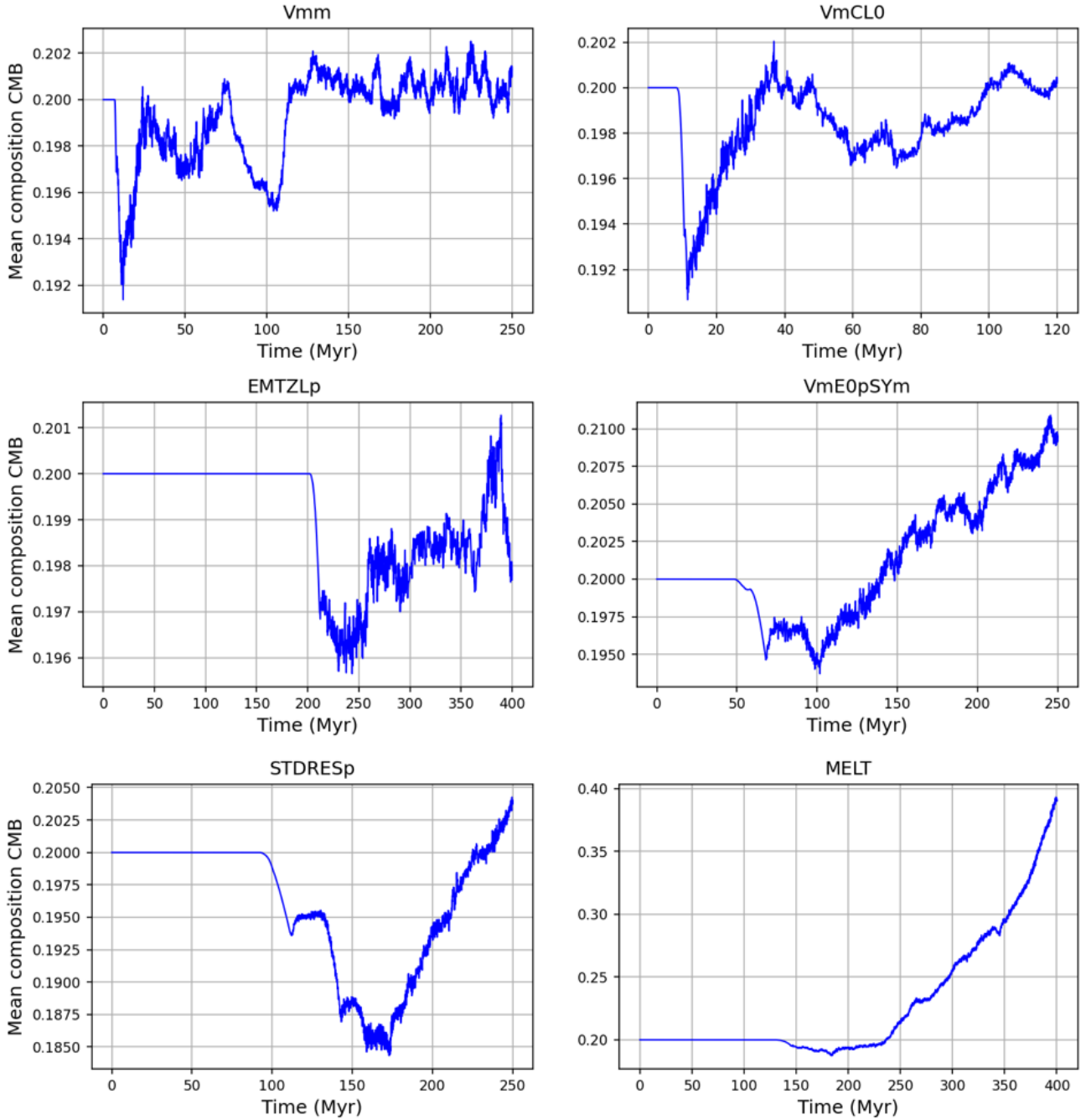


Figure A5: Evolution of basalt content near CMB for other models, continued. Models CLmed, CL0, Vmm, VmE0pSYm shows significant accumulation and preservation of basalt; models Vm, VmedCLm, VmedCLmed, EMTZLp shows accumulation but the feature is not preserved for a long period; a few models Vmmed, VmmedCLm, VmmedCLmed are unable to produce enriched basalt signature over composition index 0.201. With basalt melt switched on and with later basalt inputs, model MELT shows extreme enrichment of basalt near CMB.